

# A new invariant-based thermo-plastic model for finite deformation analysis of short fibre reinforced composites: Development and numerical aspects

A. Dean<sup>a,\*</sup>, S. Sahraee<sup>a</sup>, J. Reinoso<sup>b</sup>, R. Rolfs<sup>a</sup>

<sup>a</sup>*Institute of Structural Analysis. Leibniz Universität Hannover, Appelstr. 9A, 30167 Hannover, Germany*

<sup>b</sup>*Elasticity and Strength of Materials Group, School of Engineering. University of Seville, Camino de los Descubrimientos s/n, 41092, Seville, Spain*

---

## Abstract

A novel invariant-based thermo-plastic model for finite deformation analysis of short fibre reinforced composites is presented including aspects of its numerical implementation. The underlying concept complies with thermodynamic restrictions, allowing a robust and consistent modeling framework. The main novelties of the current investigation concern: (i) an alternative definition of the plastic potential function assuming a non-associative plastic formulation, and (ii) the update of the preferential material orientation along the thermo-plastic deformation process using a geometrically nonlinear description. On the computational side, the derivation of an internal variable formulation using an objective integration algorithm and the closed-form of the consistent tangent moduli are outlined. The performance of the proposed model is assessed with a set of numerical simulations, which demonstrate its applicability and robustness.

**Keywords:** A. Anisotropic plasticity; B. Short fiber reinforced thermoplastics; C. Thermo-mechanical coupling; C. Finite element method (FEM); D. Finite deformation

---

## 1. Introduction

Due to their excellent behavior, the use of short fibre reinforced polymer (SFRP) composites is gaining a significant importance in different applications over the last decades. This fact stems from their relative low costs, easy processing, versatile properties and excellent specific stiffness and strength ratios in comparison to metallic alloys. Such properties have motivated their gradual incorporation into the manufacturing processes of different components, with special interest in the automotive and aerospace industries whereby weight savings constitute a fundamental target. In particular, one of the most appealing SFRP composites are those comprising polyamide and short glass fiber composite materials (being denominated as PAxGF-y, where x and y denote the polyamide-type and the fiber content, respectively).

Injection moulding (IM) and extrusion compounding are commonly used manufacturing techniques to produce intricate SFRP-based components. Specifically, IM is a mass-production method which induces the anisotropic mechanical behavior and consequently it is possible to identify a preferential material direction. In this concern, several studies have revealed that IM SFRP composites have a very complex fibre arrangement over the specimen thickness with different regions (Figure 1). According to [21], two typical fibre distributions can be found in practice:

- Skin-core-skin formations in thick samples, where it is possible to identify different regions over the thickness direction in terms of the fibres orientation. In particular, these specimens comprise: the two outer skins layers (dominating the mechanical response since they represent about 90% of the thickness) with fibres mainly aligned with the flow direction [3], and a central core layer which is

---

\*Corresponding authors

Email address: adean@isd.uni-hannover.de (A. Dean)

characterized by the predominant presence of fibres transversely oriented with respect to the flow direction

- Quasi-uniform formations with thin cross sections (extensively used for characterization purposes), whereby the fibres orientation are generally coincident with the flow direction.

The determination of the preferential fibre orientation has been carried out through nondestructive experimental techniques such as optical observations, radiography procedures, CT scans, among many other techniques, see [4, 6, 49].

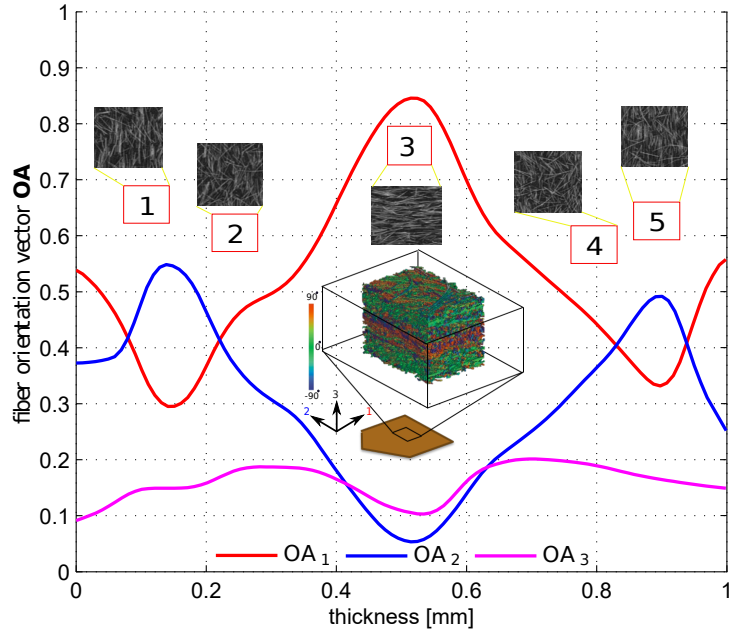


Figure 1: Micro-computed tomography of SFRP PA6GF30 processed by injection moulding procedure: distribution of the preferential material direction is shown over the specimen thickness.

The effective exploitation of the capabilities of SFRP composites demands the profound understanding of such materials under different loading scenarios and environmental conditions (including thermal, moisture and hygroscopic effects). These aspects have been comprehensively addressed in the recent literature review by Eftekhari and Fatemi [14], see also [58, 59]. In this context, previous investigations have been focused on the characterization of the corresponding tensile and compressive properties for different fibre orientations, the identification of the different damage mechanisms that govern the inelastic behavior prior to failure, the performance under fatigue loading, see [4, 8, 15, 30, 37, 55, 56, 57] among many others. These studies generally reported a characteristic nonlinear material response, especially when loading and moulding directions are not coincident. From the mechanical point of view, this evolution is mainly governed by the highly non-linear behaviour of the polymeric matrix. In addition, a major interest has been devoted to the investigation of the response of these materials under thermal actions (high temperature environments), since they greatly affect the mechanical properties of the SFRP composites when they are subjected to quasi-static and fatigue loadings, see [5, 12, 13, 33, 36].

Based on the previous considerations, numerical modeling of SFRP composites is a very challenging task. Advani and Tucker [1] (see also [2] and the references therein given) proposed a seminal mathematical formulation which encompassed the use of second and fourth order tensors in order to approximate the probability function associated with the fiber orientation. This approximation can be incorporated into FE-based simulations in a straightforward manner. Alternative refined formulations account for capturing

the nonlinear response of SFRP composites using a finer length scale through the so-called FE<sup>2</sup> methods [19, 54]. However, as was amply discussed in the related literature, one of the essential shortcoming of those multiscale techniques is the dramatic increase of the computational effort [22, 46]. Thus, modeling realistic microstructures in practical applications at component level can be hardly achieved using the current computational capabilities.

A possible modeling framework at macroscopic level can be achieved by setting up phenomenological formulations, which embody the anisotropic character of the material by means of structural vectors [7, 47]. Several investigations have shown the robustness of this approach in different engineering applications such as biomechanics [23, 18] and composites [48, 39, 38]. Other formulations of anisotropic material behaviour can be found in [34, 51] e.q. Subsequent investigations have extended these concepts to the development of anisotropic elasto-plastic formulations [16, 17, 35, 42, 43], visco-elastic and visco-plastic [41] models, and coupled thermo-mechanical formulations [24, 28, 29, 45]. However, the most of these models have been mainly focused on isotropic models. In this setting, two fundamental formulations are usually employed to thermo-mechanical analysis of solids: (i) through the use of the multiplicative decomposition of the deformation gradient considering a temperature-dependent contribution (usually denoted as  $\mathbf{F}^g$ ) [24, 31, 32], and (ii) relying on the entropic approximation, which accounts for the explicit incorporation of the temperature dependency in the definition of the Helmholtz free-energy function [25, 45].

The goal of this paper is to develop a new 3D invariant-based thermo-plastic model for finite deformation analysis of short fibre reinforced composites [10, 11, 52, 53] complying with the entropic formulation mentioned above. To account for the anisotropic response, the proposed model is based on the idea of mapping the preferential material direction of SFRP composites along the deformation process. This can substantially modify the actual specimen response in service [11]. The salient aspects of the proposed approach are: (i) the use of the multiplicative decomposition of the deformation gradient relying on the definition of a so-called intermediate configuration [17], (ii) the construction of the Helmholtz free energy function complying with the *rational thermodynamics framework* [26, 50], whereby the accommodation of the anisotropic response is defined via a tensor-based representation, (iii) the consideration of the plastic entropy as additional independent internal variable [45], and (iv) the comprehensive description of the numerical aspects with regard to the implementation within an implicit FE-scheme.

The contents of the current manuscript are organized as follows. Section 2 presents the continuous formulation of the proposed model, paying special attention to the thermodynamic restrictions and the description of the non-associative thermo-plastic formulation. On the computational side, the numerical treatment of the model exploiting the elasto-plastic return mapping algorithm at integration point level and the fully coupled global Newton-type solution scheme are outlined in Section 3. The paper concludes with a series of representative simulations in Section 4, which highlight the efficiency and accuracy of the proposed model. Finally, the main conclusions of the current investigation are summarized in Section 5.

## 2. Continuous formulation

This section outlines the basic ingredients for the development of the proposed thermo-plastic model for SFRP composites within the finite deformation setting. The goal of this section is concerned with the systematic and consistent extension of the previous models developed by the authors in [10, 11] for finite thermo-plastic analysis.

### 2.1. Kinematics

Consider a continuous body which occupies the reference placement  $\mathcal{B}_0 \subset \mathbb{R}^3$  and material points  $\mathbf{X} \in \mathcal{B}_0$ . The corresponding current position of the body is denoted by  $\mathcal{B}_t \subset \mathbb{R}^3$ , whilst the current position vector of an arbitrary point is identified by  $\mathbf{x} \in \mathcal{B}_t$ . Both configurations are related via the nonlinear motion  $\varphi : \mathcal{B}_0 \times [0, t] \rightarrow \mathbb{R}^3$ , where  $[0, t]$  denotes the time interval elapsed such that the reference material points ( $\mathbf{X} \in \mathcal{B}_0$ ) are mapped onto the current material points ( $\mathbf{x} \in \mathcal{B}_t$ ), i.e.  $\mathbf{x} = \varphi(\mathbf{X}, t)$ . Accordingly, the standard displacement vector is defined as:  $\mathbf{u} := \mathbf{x} - \mathbf{X}$ .

The definition of the deformation gradient reads:  $\mathbf{F} := \partial\varphi(\mathbf{X}, t)/\partial\mathbf{X}$ , where  $J(\mathbf{X}, t) := \det[\mathbf{F}] > 0$  denotes the Jacobian of the transformation. The polar decomposition of the deformation gradient is expressed

as:  $\mathbf{F} = \mathbf{R}\mathbf{U}$ , where  $\mathbf{R}$  and  $\mathbf{U}$  denote the rotation tensor and the stretch tensor, respectively. Furthermore, we denote  $\rho_0$  and  $\rho = J\rho_0$  as the density in the reference and current configurations, respectively.

The absolute temperature  $\vartheta : \mathcal{B}_0 \times [0, t] \rightarrow \mathbb{R}_+$  is assumed to be a smooth function of  $(\mathbf{X}, t) \in \mathcal{B}_0 \times [0, t]$  and  $\vartheta_0$  a given homogeneous reference temperature. In line with [25], the reference configuration is assumed to be stress-free.

The definition of the symmetric right and left Cauchy-Green deformation tensors,  $\mathbf{C}$  and  $\mathbf{b}$ , respectively, and the Green-Lagrange strain tensor,  $\mathbf{E}$ , are given by

$$\mathbf{C} := \mathbf{F}^T \mathbf{F}; \quad \mathbf{b} := \mathbf{F} \mathbf{F}^T; \quad \mathbf{E} := \frac{1}{2} [\mathbf{C} - \mathbf{1}], \quad (1)$$

where  $\mathbf{1}$  denotes the second-order identity tensor.

Motivated by the micro-mechanical evolution of plastic deformation, for the current phenomenological model, we assume the classic kinematic ansatz which encompasses the multiplicative decomposition of  $\mathbf{F}$  into elastic and plastic counterparts through a stress free intermediate configuration  $\bar{\mathcal{B}}$  (Figure 2) [45]:

$$\mathbf{F} = \mathbf{F}^e \mathbf{F}^p. \quad (2)$$

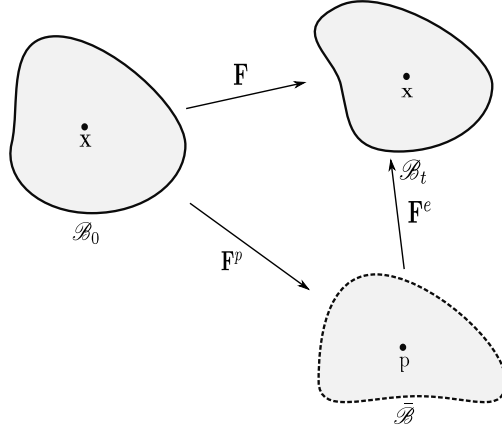


Figure 2: Intermediate configuration definition: multiplicative decomposition of the deformation gradient  $\mathbf{F} = \mathbf{F}^e \mathbf{F}^p$  for large deformation elasto-plasticity.

Based on the previous decomposition, Eq.(2), the elastic part  $\mathbf{E}^e$  of the Green-Lagrange strain tensor in the intermediate configuration takes the form

$$\mathbf{E}^e = \frac{1}{2} [\mathbf{C}^e - \mathbf{1}], \quad (3)$$

where  $\mathbf{C}^e := \mathbf{F}^{eT} \mathbf{F}^e$  stands for the elastic right Cauchy-Green strain tensor. Furthermore, assuming plastic incompressibility, the following constraint should be satisfied:

$$\det \mathbf{F}^p = 1. \quad (4)$$

Above definitions constitute an essential basis for subsequent developments.

## 2.2. Constitutive framework

At the macroscopic level, the performance of SFRP composites according to a phenomenological formulation can be approximated using a transversely anisotropic material model, which is characterized by the

preferred material direction in the reference configuration  $\mathbf{a}$ . Accordingly, the second order structural tensor  $\mathbf{A}$  which characterizes the material response is given by

$$\mathbf{A} := \mathbf{a} \otimes \mathbf{a}. \quad (5)$$

Thus, the material response is invariant with respect to arbitrary rotations around such direction, to reflections at planes parallel to  $\mathbf{a}$  and with respect to the planes whose normal vector is aligned with  $\mathbf{a}$  [7, 47]. These operations constitute the group of symmetry transformations for transverse isotropy. The current definition of the Helmholtz free-energy function includes the structural tensor introduced above.

In addition to the previous considerations, it is worth mentioning that since SFRP composites usually exhibit a nonuniform fibre distribution over the thickness, the current formulation adopts the so-called Equivalent Single Layer (ESL) approach [40]. Therefore, an averaging procedure of the fibre distribution over the cross section is performed in order to compute the ESL-properties.

The constitutive response of SFRP composites is assumed to be characterized by the Helmholtz free-energy function  $\Psi(\mathbf{E}^e, \boldsymbol{\alpha}, \vartheta, \mathbf{A})$ , which can be additively decomposed into the corresponding elastic and plastic counterparts,  $\Psi^e(\mathbf{E}^e, \vartheta, \mathbf{A})$  and  $\Psi^p(\boldsymbol{\alpha}, \vartheta, \mathbf{A})$ , respectively:

$$\Psi(\mathbf{E}^e, \boldsymbol{\alpha}, \vartheta, \mathbf{A}) = \Psi^e(\mathbf{E}^e, \vartheta, \mathbf{A}) + \Psi^p(\boldsymbol{\alpha}, \vartheta, \mathbf{A}), \quad (6)$$

where  $\boldsymbol{\alpha}$  denotes the vector of internal variables that trigger the evolution of the plastic deformation.

An analogous decomposition scheme is also adopted for the total entropy of the system  $\eta$  due to the extensive character of this quantity:

$$\eta = \eta^e + \eta^p, \quad (7)$$

where  $\eta^e$  and  $\eta^p$  denote the terms corresponding to elastic and plastic entropy, respectively. The evolution of the internal variable  $\eta^p$  contributes to the entropy production along the deformation process.

In order to represent the anisotropic constitutive functions as isotropic tensor function, the internal energy function  $e$  takes the following form:

$$e = e(\mathbf{E}^e, \mathbf{A}, \eta^e). \quad (8)$$

Recalling the standard Legendre transformation [26], one obtains

$$\Psi^e(\mathbf{E}^e, \vartheta, \mathbf{A}) = e(\mathbf{E}^e, \mathbf{A}, \eta^e) - \eta^e \vartheta. \quad (9)$$

Following the Coleman and Noll procedure [9], the following relations are derived:

$$\eta^e = -\frac{\partial \Psi^e}{\partial \vartheta}; \quad \vartheta = \frac{\partial e}{\partial \eta^e}; \quad c_p = -\vartheta \frac{\partial^2 \Psi^e}{\partial \vartheta^2} = \vartheta \frac{\partial \eta^e}{\partial \vartheta} = \frac{\partial e}{\partial \vartheta}, \quad (10)$$

where  $c_p$  stands for the specific heat capacity at constant deformation. Accordingly, from Eq.(10), one obtains

$$e = e_0 + \int_{\vartheta_0}^{\vartheta} c_p d\hat{\vartheta}; \quad \eta^e = \eta_0^e + \int_{\vartheta_0}^{\vartheta} \frac{c_p}{\hat{\vartheta}} d\hat{\vartheta}, \quad (11)$$

where  $e_0$  and  $\eta_0^e$  denote the internal energy and elastic entropy at reference temperature  $\vartheta_0$ , respectively.

The insertion of the previous expressions into Eq.(9) yields

$$\Psi^e(\mathbf{E}^e, \vartheta, \mathbf{A}) = e_0 + \int_{\vartheta_0}^{\vartheta} c_p d\hat{\vartheta} - \vartheta \left[ \eta_0^e + \int_{\vartheta_0}^{\vartheta} \frac{c_p}{\hat{\vartheta}} d\hat{\vartheta} \right] = e_0 - \vartheta \eta_0^e + T(\vartheta), \quad (12)$$

with

$$T(\vartheta) = \int_{\vartheta_0}^{\vartheta} c_p \left( 1 - \frac{\vartheta}{\hat{\vartheta}} \right) d\hat{\vartheta} \quad (13)$$

Now  $\Psi_0^e := e_0 - \vartheta\eta_0^e$  is defined as the free energy of an isothermal process with constant reference temperature. Then, the elastic contribution to the free energy  $\Psi^e(\mathbf{E}^e, \vartheta, \mathbf{A})$  can be determined as follows:

$$\Psi^e(\mathbf{E}^e, \vartheta, \mathbf{A}) = \frac{\vartheta}{\vartheta_0} \Psi_0^e + e_0 \left(1 - \frac{\vartheta}{\vartheta_0}\right) + T(\vartheta), \quad (14)$$

where  $e_0 \left(1 - \frac{\vartheta}{\vartheta_0}\right)$  is the thermo-mechanical contribution and  $T(\vartheta)$  denotes the fully thermal contribution.

The mechanical contribution at reference temperature is constructed from the following irreducible integrity basis  $\mathcal{P} := [J_1, \dots, J_4]$  assuming a quadratic form. The invariants  $J_1$  and  $J_2$  are defined by

$$J_1 := \text{tr}[\mathbf{E}^e]; \quad J_2 := \text{tr}[(\mathbf{E}^e)^2], \quad (15)$$

whereas the mixed invariants  $J_3$  and  $J_4$  are given by

$$J_3 := \text{tr}[\mathbf{A}\mathbf{E}^e]; \quad J_4 := \text{tr}[\mathbf{A}(\mathbf{E}^e)^2]. \quad (16)$$

The particular form of the elastic free energy function is assumed to obey the following expression:

$$\Psi_0^e(\mathbf{E}^e, \vartheta, \mathbf{A}) = \frac{\lambda}{2} J_1^2 + \mu_T J_2 + \alpha J_3 J_1 + 2(\mu_L - \mu_T) J_4 + \frac{\beta}{2} J_3^2 = \frac{1}{2} \mathbf{E}^e : \mathbb{C}_0^e : \mathbf{E}^e, \quad (17)$$

where  $\lambda, \mu_L, \mu_T, \alpha, \beta$  denote the elastic constants, see [10, 52].

The elasticity tensor  $\mathbb{C}_0^e$  at reference temperature  $\vartheta_0$  is given by

$$\mathbb{C}_0^e := \frac{\partial^2 \Psi_0^e}{\partial \mathbf{E}^{e,2}} = \lambda \mathbf{1} \otimes \mathbf{1} + 2\mu_T \mathbb{I} + \alpha (\mathbf{1} \otimes \mathbf{A} + \mathbf{A} \otimes \mathbf{1}) + 2(\mu_L - \mu_T) \mathbb{I}_{\mathbf{A}} + \beta \mathbf{A} \otimes \mathbf{A}, \quad (18)$$

where  $\mathbb{I}$  denotes the fourth-order symmetric identity tensor and  $\mathbb{I}_{\mathbf{A}}$  is expressed as follows:

$$\mathbb{I}_{\mathbf{A}} \Rightarrow \mathbb{I}_{\mathbf{A},ijkl} = \mathbf{A}_{im} \mathbb{I}_{jmk} + \mathbf{A}_{jm} \mathbb{I}_{mik}. \quad (19)$$

The isotropic thermal expansion,  $e_0$  is given by the following relationship [24]:

$$e_0 = 3\xi k_0 \vartheta_0 \ln J^e, \quad (20)$$

where  $\xi, k_0$  and  $J^e$  denote the thermal expansion coefficient, bulk modulus and Jacobian of  $\mathbf{F}^e$ , respectively.

For a generic anisotropic material, the thermal expansion,  $e_0$ , can be expressed as

$$e_0 = c^* \ln J^e, \quad (21)$$

where  $c^*$  is a suitable operator.

### 2.3. The reduced dissipation inequality

The consistency of the proposed formulation is examined through the exploitation of the Clausius-Plank inequality for internal dissipation,  $\mathcal{D}_{\text{int}}$ :

$$\mathcal{D}_{\text{int}} = \mathbf{S} : \dot{\mathbf{E}} - \dot{\mathbf{e}} + \vartheta \dot{\eta} \geq 0, \quad (22)$$

where  $\mathbf{S}$  and  $\dot{\mathbf{E}}$  represent the Second Piola-Kirchhoff stress tensor and the material time derivative of the Green-Lagrange strain tensor, respectively.

Through the adoption of the multiplicative decomposition of the deformation gradient, Eq.(2), the internal dissipation reads:

$$\mathcal{D}_{\text{int}} = \mathbf{S} : \left( \frac{1}{2} \mathbf{F}^{pT} \dot{\mathbf{C}}^e \mathbf{F}^p + \mathbf{F}^{pT} (\mathbf{C}^e \mathbf{L}^p)_s \mathbf{F}^p \right) - \dot{\Psi} - \eta^e \dot{\vartheta} + \vartheta \dot{\eta}^p \geq 0, \quad (23)$$

where  $\mathbf{L}^p = \dot{\mathbf{F}}^p \mathbf{F}^{p-1}$  denotes the plastic velocity gradient which is decomposed into its symmetric  $\mathbf{D}^p$  (plastic deformation rate) and skew-symmetric  $\mathbf{W}^p$  (plastic material spin) parts as follows:

$$\mathbf{L}^p = \mathbf{D}^p + \mathbf{W}^p. \quad (24)$$

Inserting the previous definitions into Eq.(23), one obtains

$$\mathcal{D}_{\text{int}} = \frac{1}{2} \bar{\mathbf{S}} : \dot{\mathbf{C}}^e + \bar{\mathbf{S}} : (\mathbf{C}^e \mathbf{L}^p)_s - \dot{\Psi}^e - \eta^e \dot{\vartheta} - \dot{\Psi}^p + \vartheta \dot{\eta}^p \geq 0, \quad (25)$$

where  $\bar{\mathbf{S}} = \mathbf{F}^p \mathbf{S} \mathbf{F}^{pT}$  stands for the Second Piola-Kirchhoff stress tensor counterpart in the intermediate configuration.

Accordingly,

$$\mathcal{D}_{\text{int}} = \left( \frac{1}{2} \bar{\mathbf{S}} - \frac{\partial \Psi^e}{\partial \mathbf{C}^e} \right) : \dot{\mathbf{C}}^e + (\mathbf{C}^e \bar{\mathbf{S}}) : \mathbf{L}^p - \left( \frac{\partial \Psi^e}{\partial \vartheta} + \eta^e \right) \dot{\vartheta} - \dot{\psi}^p + \vartheta \dot{\eta}^p \geq 0. \quad (26)$$

Therefore, according to the standard Coleman and Noll procedure aforementioned, the following constitutive equations are obtained:

$$\bar{\mathbf{S}} = 2 \frac{\partial \Psi^e}{\partial \mathbf{C}^e} = \frac{\vartheta}{\vartheta_0} (\mathbb{C}_0^e : \mathbf{E}^e) + c^* \left( 1 - \frac{\vartheta}{\vartheta_0} \right) \mathbf{C}^{e-1}, \quad (27)$$

$$\eta^e = - \frac{\partial \Psi^e}{\partial \vartheta} = - \frac{1}{\vartheta_0} \Psi_0^e + \frac{1}{\vartheta_0} e_0 + T'(\vartheta) = - \frac{1}{\vartheta_0} (\Psi_0^e - e_0) + T'(\vartheta). \quad (28)$$

#### 2.4. Heat conduction

To complete the current formulation, the corresponding equation for heat conduction is required. A suitable constitutive equation that complies with experimental observations is Fourier's law of heat conduction, which in the current configuration is given by

$$\mathbf{q} = -\mathbf{k}(\vartheta) \nabla_{\mathbf{x}} \vartheta, \quad (29)$$

where  $\mathbf{q}$  denotes the Cauchy heat flux,  $\mathbf{k}(\vartheta)$  is the second-order heat conductivity tensor, and  $\nabla_{\mathbf{x}} \vartheta$  stands for the spatial gradient of the temperature. The restricted claim for the conductivity renders:  $\mathbf{q} \nabla_{\mathbf{x}} \vartheta \leq 0$ .

The consistency of the formulation with regard to the Helmholtz free energy function in the reference configuration is preserved by means of computing the material form of the heat flux using Nanson's formula:  $\mathbf{Q} = J \mathbf{F}^{-1} \mathbf{q}$ .

Based on the previous considerations, the restriction with regard to the local internal dissipation in order to fulfill the second law of thermodynamics is reduced to:

$$\mathcal{D}_{\text{int}} = \bar{\Sigma} : \mathbf{L}^p - \dot{\Psi}^p + \vartheta \dot{\eta}^p \geq 0, \quad (30)$$

where  $\bar{\Sigma} = \mathbf{C}^e \bar{\mathbf{S}}$  denotes the so-called Mandel stress tensor.

Furthermore, the local dissipation can be written as additive decomposition of a mechanical  $\mathcal{D}_{\text{int}}^{\text{mech}}$  and a thermal  $\mathcal{D}_{\text{int}}^{\text{th}}$  contributions as follows

$$\mathcal{D}_{\text{int}} = \mathcal{D}_{\text{int}}^{\text{mech}} + \mathcal{D}_{\text{int}}^{\text{th}}, \quad (31)$$

with

$$\mathcal{D}_{\text{int}}^{\text{mech}} = \bar{\Sigma} : \mathbf{L}^p - \dot{\Psi}^p; \quad \mathcal{D}_{\text{int}}^{\text{th}} = \vartheta \dot{\eta}^p. \quad (32)$$

## 2.5. Transversely isotropic yield function

Henceforth, the construction of the transversely isotropic yield function which characterizes the plastic locus of the current model is presented. It is worth mentioning that the following developments rely on the previous model proposed by the authors in [10, 11].

The thermo-elastic domain  $\mathbb{E}$  is specified in a standard format in terms of the Mandel stress tensor  $\bar{\Sigma}$  previously defined as follows:

$$\mathbb{E} = \{(\bar{\varepsilon}, \vartheta) | f(\bar{\Sigma}_s, \mathbf{A}, \bar{\varepsilon}, \vartheta) \leq 0\}, \quad (33)$$

where  $\bar{\Sigma}_s$  denotes the symmetric part of Mandel stress tensor and  $\bar{\varepsilon}$  identifies the equivalent plastic strain (hardening variable) whose evolution equation is given by

$$\dot{\bar{\varepsilon}} = \sqrt{\frac{2}{3}\mathbf{D}^p : \mathbf{D}^p}. \quad (34)$$

The construction of a quadratic, temperature and pressure dependent, transversely isotropic and asymmetric yield surface  $f(\bar{\Sigma}_s, \mathbf{A}, \bar{\varepsilon}, \vartheta) \leq 0$  can be expressed as:

$$f(\bar{\Sigma}_s, \mathbf{A}, \bar{\varepsilon}, \vartheta) = \zeta_1 I_1 + \zeta_2 I_2 + \zeta_3 I_3 + \zeta_4 I_3^2 + \zeta_5 I_4 + \zeta_6 I_4^2 - 1 \leq 0 \quad \text{with} \quad \mathbf{n}_f := \frac{\partial f}{\partial \bar{\Sigma}}, \quad (35)$$

where  $I_i$  ( $i = 1, 4$ ) identifies the integrity basis (invariants) as the transversely isotropic yield function  $f$  is formulated as an isotropic tensor function, and  $\mathbf{n}_f$  denotes the normal vector to the yield surface. The particular form of these invariants reads

$$I_1 := \text{tr} \left[ \left( \bar{\Sigma}_s^{pind} \right)^2 \right] - \text{tr} \left[ \mathbf{A} \left( \bar{\Sigma}_s^{pind} \right)^2 \right]; \quad I_2 := \text{tr} \left[ \mathbf{A} \left( \bar{\Sigma}_s^{pind} \right)^2 \right]; \quad I_3 := \text{tr} [\bar{\Sigma}_s] - \text{tr} [\mathbf{A} \bar{\Sigma}_s]; \quad I_4 := \frac{3}{2} \text{tr} [\mathbf{A} \bar{\Sigma}_s^{dev}], \quad (36)$$

where  $\bar{\Sigma}_s^{dev}$  identifies the deviatoric part of the symmetric Mandel stress tensor, whereas  $\bar{\Sigma}_s^{pind}$  denotes the basic stress that induces plasticity [52]:

$$\bar{\Sigma}_s^{pind} = \bar{\Sigma}_s - \frac{1}{2} (\text{tr} [\bar{\Sigma}_s] - \text{tr} [\mathbf{A} \bar{\Sigma}_s]) \mathbf{1} + \frac{1}{2} (\text{tr} [\bar{\Sigma}_s] - 3 \text{tr} [\mathbf{A} \bar{\Sigma}_s]) \mathbf{A}. \quad (37)$$

The six temperature dependent parameters  $\zeta_i(\bar{\varepsilon}, \vartheta)$ , ( $i = 1, 6$ ) and their corresponding invariants represent different thermo-mechanical loading states. In line with [10, 11], the following interpretation of these parameters can be identified: (1)  $\zeta_1$  is associated with transverse shear loading states, (2)  $\zeta_2$  considers in-plane shear loading. (3)  $\zeta_3$  and  $\zeta_4$  account for thermo-mechanical loading transverse to the fiber direction, and finally (4)  $\zeta_5$  and  $\zeta_6$  characterize the material response associated with longitudinal loading along the fibre direction.

The proposed yield function can be represented in condensed format as

$$f(\bar{\Sigma}_s, \mathbf{A}, \bar{\varepsilon}, \vartheta) = \frac{1}{2} \bar{\Sigma}_s : \mathbb{K} : \bar{\Sigma}_s + \mathbf{L} : \bar{\Sigma}_s - 1 \leq 0, \quad (38)$$

with

$$\mathbb{K} := \zeta_1 \mathbb{P}^{pind} + (\zeta_2 - \zeta_1) \mathbb{P}_{\mathbf{A}}^{pind} + 2\zeta_4 (\mathbf{1} - \mathbf{A}) \otimes (\mathbf{1} - \mathbf{A}) + \frac{9}{2} \zeta_6 \mathbf{A}^{dev} \otimes \mathbf{A}^{dev}, \quad (39)$$

$$\mathbf{L} := \zeta_3 (\mathbf{1} - \mathbf{A}) + \frac{3}{2} \zeta_5 \mathbf{A}^{dev}, \quad (40)$$

$$\mathbb{P}^{pind} := \mathbb{I} - \frac{1}{2} (\mathbf{1} \otimes \mathbf{1}) + \frac{1}{2} (\mathbf{1} \otimes \mathbf{A} + \mathbf{A} \otimes \mathbf{1}) - \frac{3}{2} \mathbf{A} \otimes \mathbf{A}, \quad (41)$$

$$\mathbb{P}_{\mathbf{A}}^{pind} \Rightarrow \mathbb{P}_{\mathbf{A},ijkl}^{pind} = \mathbf{A}_{im} \mathbb{P}_{mkl}^{pind} + \mathbf{A}_{mj} \mathbb{P}_{imkl}^{pind}, \quad (42)$$

where  $\mathbf{A}^{dev}$  is the deviatoric part of the structural tensor  $\mathbf{A}$ .

A 3D representation in the principal stress space and a series of cross sections in the invariant space of the yield surface in the invariant space are shown in Figure 3. In these graphs, the convex form of the yield surface can be observed along with the interaction between different loading states relying on the invariant representation.

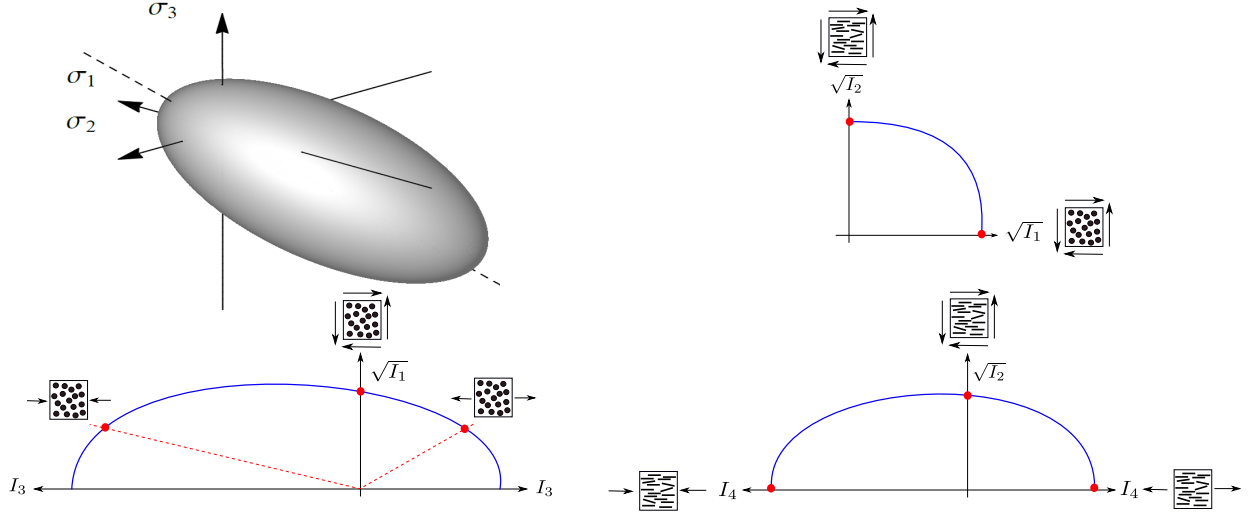


Figure 3: Transversely isotropic yield function: 3D representation in the principal stress space and cross sections in the invariant space.

### 2.6. Plastic potential function

Recalling the plastic incompressibility assumption, Eq.(4), the current model introduces the definition of a non-associative flow rule. This leads to the definition of the temperature dependent plastic potential  $g = g(\bar{\Sigma}_s, \mathbf{A}, \vartheta)$ . Analogously to the formulation of the yield surface, the anisotropic plastic potential function  $g$  is formulated as an isotropic tensor function as follows:

$$g(\bar{\Sigma}_s, \mathbf{A}, \vartheta) = \iota_1 \bar{I}_1 + \iota_2 \bar{I}_2 - 1 \leq 0, \quad (43)$$

where  $\bar{I}_1$  and  $\bar{I}_2$  stand for the following integrity basis (invariants):

$$\bar{I}_1 := \text{tr} \left[ \left( \bar{\Sigma}_s^{dev} \right)^2 \right]; \quad \bar{I}_2 := \text{tr} \left[ \mathbf{A} \left( \bar{\Sigma}_s^{dev} \right)^2 \right], \quad (44)$$

where  $\iota_1$  and  $\iota_2$  denote the temperature dependent plastic potential parameters [10].

In condensed form, the plastic flow potential  $g$  can be expressed as:

$$g(\bar{\Sigma}_s, \mathbf{A}, \vartheta) = \frac{1}{2} \bar{\Sigma}_s : \mathbb{M} : \bar{\Sigma}_s - 1 \leq 0, \quad (45)$$

with

$$\mathbb{M} := 2\iota_1 \mathbb{I}^{dev} + \iota_2 \mathbb{I}_{\mathbf{A}}^{dev}; \quad \mathbb{I}^{dev} := \mathbb{I} - \frac{1}{3} \mathbf{1} \otimes \mathbf{1}; \quad \mathbb{I}_{\mathbf{A}}^{dev} \Rightarrow \mathbb{I}_{\mathbf{A},klmn}^{dev} = \mathbf{A}_{ij} (\mathbb{I}_{jsmn}^{dev} \mathbb{I}_{sikl}^{dev} + \mathbb{I}_{jskl}^{dev} \mathbb{I}_{simn}^{dev}). \quad (46)$$

Figure 4 depicts a cross section of the plastic potential in the invariant space and a 3D representation in the principal stress space.

### 2.7. Evolution equations of the internal variables

Through the invocation of the maximum energy dissipation principle [45] and using the non-associative flow rule introduced in Section 2.6, the evolution equations of the internal variables, namely the plastic velocity gradient  $\mathbf{L}^p$ , the hardening variable  $\bar{\epsilon}$  and the plastic entropy  $\eta^p$  are defined as follows:

$$\mathbf{L}^p = \mathbf{D}^p = \dot{\gamma} \frac{\partial g(\bar{\Sigma}_s, \mathbf{A}, \vartheta)}{\partial \bar{\Sigma}_s} = \dot{\gamma} \mathbf{n}_g \quad \text{with} \quad \mathbf{n}_g = \mathbb{M} : \bar{\Sigma}_s, \quad (47)$$

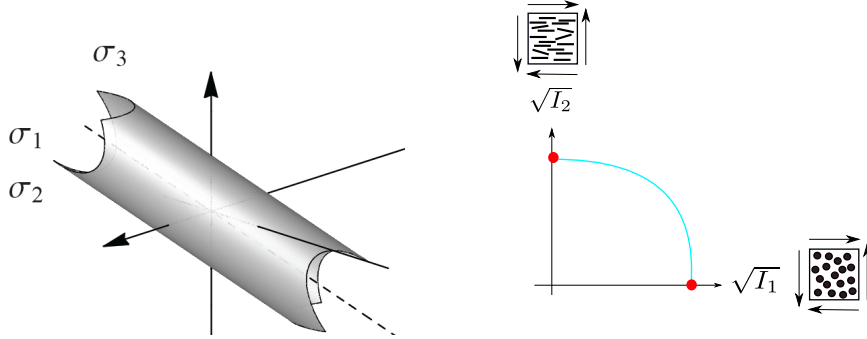


Figure 4: Plastic potential function: 3D representation in the principal stress space and cross sections in the invariant space.

$$\dot{\epsilon} = \sqrt{\frac{2}{3} \mathbf{D}^p : \mathbf{D}^p} = \dot{\gamma} \sqrt{\frac{2}{3}} \|\mathbf{n}_g\|, \quad (48)$$

$$\dot{\eta}^p = \dot{\gamma} \frac{\partial g(\bar{\Sigma}_s, \mathbf{A}, \vartheta)}{\partial \vartheta} = \dot{\gamma} g_\vartheta \quad \text{with} \quad g_\vartheta = \frac{1}{2} \bar{\Sigma}_s : \mathbb{M}_\vartheta : \bar{\Sigma}_s, \quad (49)$$

where  $\dot{\gamma}$  identify the so-called plastic multiplier and  $\mathbb{M}_\vartheta = \frac{\partial \mathbb{M}}{\partial \vartheta}$ .

Since solely the symmetric part of the Mandel stress tensor enters into the plastic potential function, the plastic material spin in the intermediate configuration  $\mathbf{W}^p$  vanishes. As a consequence of this fact, the constitutive equations are invariant with respect to any arbitrary rigid body rotation  $\bar{\mathbf{Q}}$ , which can be superimposed onto the intermediate configuration. This condition can be expressed as:

$$\mathcal{O} \rightarrow \bar{\mathbf{Q}} \mathcal{O}^* \bar{\mathbf{Q}}^T \quad \text{for} \quad \mathcal{O} = \{\mathbf{C}^e, \bar{\mathbf{S}}, \bar{\Sigma}, \mathbf{D}^p\}. \quad (50)$$

The standard Kuhn-Tucker loading/unloading conditions read

$$\dot{\gamma} \geq 0; \quad f(\bar{\Sigma}_s, \mathbf{A}, \bar{\epsilon}, \vartheta) \leq 0; \quad \dot{\gamma} f(\bar{\Sigma}_s, \mathbf{A}, \bar{\epsilon}, \vartheta) = 0. \quad (51)$$

Finally, the consistency condition is given by

$$\dot{\gamma} \dot{f}(\bar{\Sigma}_s, \mathbf{A}, \bar{\epsilon}, \vartheta) = 0. \quad (52)$$

### 2.8. Parameter identification

The characterization of the proposed thermo-plastic model requires the determination of material parameters that define the proposed yield surface, Eq.(35), and plastic potential function, Eq.(43). This procedure can be performed according to the description discussed in [10]. Consequently, a brief description is considered herein for the sake of completeness.

First, with regard to the six independent yield surface parameters  $(\zeta_i(\bar{\epsilon}, \vartheta), (i = 1, 6))$ , they can be experimentally identified by means of the following six different independent tests: (i) in-plane shear test, (ii) transverse shear test, (iii) uniaxial longitudinal tension and compression tests, and (iv) uniaxial transverse tension and compression tests.

At this point, a clarifying remark regarding the convexity of the yield surface is worth to be addressed. First, as a result of the invocation maximum energy dissipation principle, the yield surface is convex. Such convex character of the yield surface  $f(\bar{\Sigma}_s, \mathbf{A}, \bar{\epsilon}, \vartheta)$  is ensured if and only if  $f''(\bar{\Sigma}_s, \mathbf{A}, \bar{\epsilon}, \vartheta) \geq 0$ . As a consequence, the following condition should hold:

$$Y_{ucf} Y_{utf} (4Y_{str}^2 - Y_{uct} Y_{utt}) \geq Y_{uct} Y_{str}^2 Y_{utt}, \quad (53)$$

where  $Y_{utf}$ ,  $Y_{ucf}$ ,  $Y_{utt}$ ,  $Y_{uct}$ ,  $Y_{str}$  denote uniaxial longitudinal tension, uniaxial longitudinal compression, uniaxial transverse tension, uniaxial transverse compression and transverse shear yield strengths, respectively.

Second, with reference to the plastic potential function, the motivating reason for using a non-associative flow rule is the determination of realistic plastic deformation behavior, especially in terms of the so-called plastic Poisson's ratio  $\nu^p$ . Consequently, in order to determine the plastic potential parameters  $\iota_1$  and  $\iota_2$  that yield the desired plastic Poisson's ratio, a simple trial and error optimization procedure is employed, as described in [10, 11]. Performing such procedure, the following explicit form of the plastic potential coefficients can be obtained:

$$\iota_1 = -\frac{1}{2z_f^2} + \frac{2}{z_t^2} \text{ and; } \iota_2 = \frac{3}{z_f^2} - \frac{3}{z_t^2}, \quad (54)$$

where  $z_f$  and  $z_t$  identify the so-called potential stresses, see [10, 11] for the corresponding definitions.

### 3. Numerical treatment

The construction of a numerical scheme for the solution of the initial boundary value problem (IBVP) associated with the current thermo-plastic involves two principal steps: (i) the local integration of the transversely isotropic thermo-plastic model via the corresponding return mapping algorithm, (ii) the introduction of the result stemming from previous step is employed in the constitutive block of the weak formulation of the coupled thermo-mechanical problem, which is discretized in space by means of FEM and solved by means of a standard incremental-iterative Newton-Raphson scheme.

#### 3.1. Return mapping algorithm: local IBVP for transversely anisotropic thermo-plasticity

The central concept for the local integration of the local initial boundary value problem (IBVP) is the backward Euler procedure in order to trigger the update of the internal variables of the model. This solution process is performed using the so-called operator split (predictor-corrector) with a general return mapping, see [17, 45].

Let to consider a time interval  $[t_n, t_{n+1}^{(i)}]$ , with  $t \in \mathbb{R}_+$ , where  $t_n$  and  $t_{n+1}^{(i)}$  denote the previous converged time step and the current prospective time step at the global Newton-Raphson iteration  $i$ , respectively. In the following development, the superscript  $i$  is omitted to simplify the notation and we denote:  $\Delta t = t_{n+1}^{(i)} - t_n$ . We assume that all the variables of the problem at  $t_n$  are known.

The rates of the plastic deformation gradient, the equivalent plastic strain, the temperature and the plastic entropy within the given time step render

$$\dot{\mathbf{F}}^p = \frac{\mathbf{F}_{n+1}^p - \mathbf{F}_n^p}{\Delta t}; \quad \dot{\bar{\epsilon}} = \frac{\bar{\epsilon}_{n+1} - \bar{\epsilon}_n}{\Delta t}; \quad \dot{\vartheta} = \frac{\vartheta_{n+1} - \vartheta_n}{\Delta t}; \quad \dot{\eta}^p = \frac{\eta_{n+1}^p - \eta_n^p}{\Delta t}. \quad (55)$$

The discrete incremental forms of the evolution equations of the internal variables comply with the backward Euler procedure:

$$\mathbf{F}_{n+1}^p = \mathbf{F}_n^p + \gamma_{n+1} \mathbf{n}_{g,n+1} \mathbf{F}_{n+1}^p \quad (56)$$

$$\bar{\epsilon}_{n+1} = \bar{\epsilon}_n + \gamma_{n+1} \sqrt{\frac{2}{3}} \|\mathbf{n}_{g,n+1}\| \quad (57)$$

$$\eta_{n+1}^p = \eta_n^p + \gamma_{n+1} g_{\vartheta,n+1} \quad (58)$$

$$f_{n+1} = f(\bar{\Sigma}_{s,n+1}, \mathbf{A}, \bar{\epsilon}_{n+1}, \vartheta_{n+1}) = 0, \quad (59)$$

where  $\gamma_{n+1}$  denotes the consistency parameter (plastic multiplier).

The first step of the predictor-corrector algorithm consists of assuming an initial purely elastic trial increment (denoted by the superscript  $tr$  in the sequel). Therefore, the computation of the trial elastic deformation gradient  $\mathbf{F}_{n+1}^{e,tr}$  reads:

$$\mathbf{F}_{n+1}^{e,tr} = \mathbf{F}_{n+1} \mathbf{F}_n^{p-1}. \quad (60)$$

Based on Eq.(60), the following operators can be defined:

$$\mathbf{C}_{n+1}^{e,tr} = \mathbf{F}_{n+1}^{e,trT} \mathbf{F}_{n+1}^{e,tr} \quad (61)$$

$$\mathbf{E}_{n+1}^{e,tr} = \frac{1}{2} [\mathbf{C}_{n+1}^{e,tr} - \mathbf{1}] \quad (62)$$

$$\bar{\mathbf{S}}_{n+1}^{tr} = \frac{\vartheta_{n+1}}{\vartheta_0} (\mathbb{C}_0^e : \mathbf{E}_{n+1}^{e,tr}) + c^* \left( 1 - \frac{\vartheta_{n+1}}{\vartheta_0} \right) \mathbf{C}_{n+1}^{e,tr-1} \quad (63)$$

$$\bar{\Sigma}_{n+1}^{tr} = \mathbf{C}_{n+1}^{e,tr} \bar{\mathbf{S}}_{n+1}^{tr}. \quad (64)$$

Through the exploitation of Eqs.(56) and (60), one obtains

$$\mathbf{F}_{n+1}^e = \mathbf{F}_{n+1}^{e,tr} (\mathbf{1} - \gamma_{n+1} \mathbf{n}_{g,n+1}). \quad (65)$$

Accordingly, the evaluation of the yield function using the current trial elastic increment renders:

$$f_{n+1}^{tr} \left( \bar{\Sigma}_{s,n+1}^{tr}, \mathbf{A}, \bar{\epsilon}_{n+1}^{tr}, \vartheta_{n+1} \right) = \frac{1}{2} \bar{\Sigma}_{s,n+1}^{tr} : \mathbb{K}_{n+1}^{tr} : \bar{\Sigma}_{s,n+1}^{tr} + \mathbf{L}_{n+1}^{tr} : \bar{\Sigma}_{s,n+1}^{tr} - 1 \leq 0, \quad (66)$$

where the operators  $\mathbb{K}^{tr}$  and  $\mathbf{L}^{tr}$  are functions of  $\zeta_i^{tr} = \zeta_i(\bar{\epsilon}_{n+1}^{tr}, \vartheta_{n+1})$ , ( $i = 1, 6$ ).

As customary, if the predictor elastic trial state lies satisfies  $f_{n+1}^{tr} \left( \bar{\Sigma}_{s,n+1}^{tr}, \mathbf{A}, \bar{\epsilon}_{n+1}^{tr}, \vartheta_{n+1} \right) \leq 0$ , this trial increment is assumed as solution of the local IBVP stated above. Conversely, a subsequent plastic corrector step is performed, which can be formulated as follows:

$$\mathbf{F}_{n+1}^e = \mathbf{F}_{n+1}^{e,tr} (\mathbf{1} - \gamma_{n+1} \mathbf{n}_{g,n+1}) \quad (67)$$

$$\bar{\epsilon}_{n+1} = \bar{\epsilon}_n + \gamma_{n+1} \sqrt{\frac{2}{3}} \|\mathbf{n}_{g,n+1}\| \quad (68)$$

$$\eta_{n+1}^p = \eta_n^p + \gamma_{n+1} g_{\vartheta,n+1} \quad (69)$$

$$f_{n+1} = f \left( \bar{\Sigma}_{s,n+1}, \mathbf{A}, \bar{\epsilon}_{n+1}, \vartheta_{n+1} \right) = 0, \quad (70)$$

where Eq.(70) represents the yield criterion as an algebraic constraint. The discrete algebraic equations outlined in Eqs.(67)-(70) constitute a system of 12 nonlinear equations with 12 unknowns, which are solved simultaneously using a standard local Newton-Raphson procedure.

The residual equations  $\mathbf{R}_{n+1} = \left\{ \mathbf{R}_{\mathbf{F}_{n+1}^e}, \mathbf{R}_{\bar{\epsilon}_{n+1}}, \mathbf{R}_{\eta_{n+1}^p}, \mathbf{R}_{f_{n+1}} \right\}$  of the system above can be cast as follows

$$\mathbf{R}_{\mathbf{F}_{n+1}^e} = \mathbf{F}_{n+1}^e - \mathbf{F}_{n+1}^{e,tr} (\mathbf{1} - \gamma_{n+1} \mathbf{n}_{g,n+1}) = \mathbf{0} \quad (71)$$

$$\mathbf{R}_{\bar{\epsilon}_{n+1}} = \bar{\epsilon}_{n+1} - \left( \bar{\epsilon}_n + \gamma_{n+1} \sqrt{\frac{2}{3}} \|\mathbf{n}_{g,n+1}\| \right) = 0 \quad (72)$$

$$\mathbf{R}_{\eta_{n+1}^p} = \eta_{n+1}^p - (\eta_n^p + \gamma_{n+1} g_{\vartheta,n+1}) = 0 \quad (73)$$

$$\mathbf{R}_{f_{n+1}} = f_{n+1} = f \left( \bar{\Sigma}_{s,n+1}, \mathbf{A}, \bar{\epsilon}_{n+1}, \vartheta_{n+1} \right) = 0 \quad (74)$$

The previous system is solved for the internal variables of the thermo-plastic problem, which are arranged in the following vector:  $\boldsymbol{\chi}_{n+1} = \left\{ \mathbf{F}_{n+1}^e, \bar{\epsilon}_{n+1}, \eta_{n+1}^p, \gamma_{n+1} \right\}$ .

The linearization of the residual equations  $\mathbf{R}_{n+1}$  above with respect to  $\boldsymbol{\chi}_{n+1}$  yields

$$\mathbf{R}_{n+1} (\boldsymbol{\chi}_{n+1}^{k+1}) := \mathbf{R}_{n+1} (\boldsymbol{\chi}_{n+1}^k) + \mathbf{J} (\boldsymbol{\chi}_{n+1}^k) [\boldsymbol{\chi}_{n+1}^{k+1} - \boldsymbol{\chi}_{n+1}^k] = \mathbf{0}, \quad (75)$$

where the superscript  $k$  identifies the Newton-Raphson iteration index corresponding to the plastic corrector step of the present procedure.

In Eq.(75), the Jacobian  $\mathbf{J}$  takes the form:

$$\mathbf{J} = \begin{bmatrix} \frac{\partial \mathbf{R}_{\mathbf{F}^e}}{\partial \mathbf{F}^e} & \frac{\partial \mathbf{R}_{\mathbf{F}^e}}{\partial \bar{\epsilon}} & \frac{\partial \mathbf{R}_{\mathbf{F}^e}}{\partial \eta^p} & \frac{\partial \mathbf{R}_{\mathbf{F}^e}}{\partial \gamma} \\ \frac{\partial \mathbf{R}_{\bar{\epsilon}}}{\partial \mathbf{F}^e} & \frac{\partial \mathbf{R}_{\bar{\epsilon}}}{\partial \bar{\epsilon}} & \frac{\partial \mathbf{R}_{\bar{\epsilon}}}{\partial \eta^p} & \frac{\partial \mathbf{R}_{\bar{\epsilon}}}{\partial \gamma} \\ \frac{\partial \mathbf{R}_{\eta^p}}{\partial \mathbf{F}^e} & \frac{\partial \mathbf{R}_{\eta^p}}{\partial \bar{\epsilon}} & \frac{\partial \mathbf{R}_{\eta^p}}{\partial \eta^p} & \frac{\partial \mathbf{R}_{\eta^p}}{\partial \gamma} \\ \frac{\partial \mathbf{R}_f}{\partial \mathbf{F}^e} & \frac{\partial \mathbf{R}_f}{\partial \bar{\epsilon}} & \frac{\partial \mathbf{R}_f}{\partial \eta^p} & \frac{\partial \mathbf{R}_f}{\partial \gamma} \end{bmatrix}. \quad (76)$$

Using the increment of the unknowns, one finds

$$\Delta \boldsymbol{\chi}_{n+1}^{k+1} := \boldsymbol{\chi}_{n+1}^{k+1} - \boldsymbol{\chi}_{n+1}^k = -\mathbf{J}^{-1}(\boldsymbol{\chi}_{n+1}^k) \mathbf{R}_{n+1}(\boldsymbol{\chi}_{n+1}^k), \quad (77)$$

where the initial values for the plastic corrector procedure are the results obtained from the elastic predictor step

$$\boldsymbol{\chi}_{n+1}^{k=0} = \begin{bmatrix} \mathbf{F}_{n+1}^{e,tr} \\ \bar{\epsilon}_n \\ \eta_n^p \\ 0 \end{bmatrix}. \quad (78)$$

The closed form of the derivatives in Eq.(78) are outlined in Appendix A. An schematic representation of the return mapping algorithm herein described is shown in Figure 5.

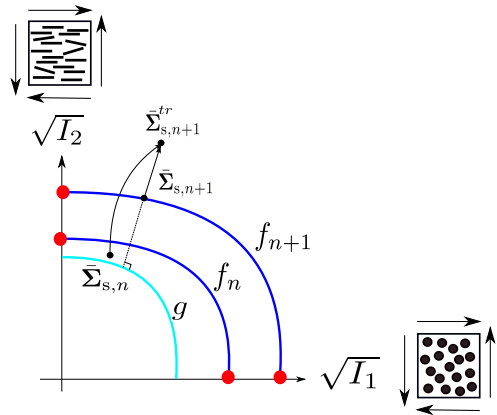


Figure 5: Return mapping algorithm: graphical description in the invariant space.

### 3.2. Algorithmic consistent tangent moduli

Using an implicit FE formulation, the computation of the algorithmic consistent tangent moduli, guarantees the quadratic convergence along the incremental-iterative solution process. Therefore, we assume that the Mandel stress tensor  $\bar{\Sigma}_{n+1}$  is determined according to the procedure outlined in Section 3.1.

Recalling Eq.(67), one obtains

$$\mathbf{F}^e = \mathbf{F}^{e,tr} (\mathbf{1} - \gamma \mathbf{n}_g) = \mathbf{F}^{e,tr} \mathbf{F}_*^p; \quad \text{with} \quad \mathbf{F}_*^{p-1} \mathbf{F}_*^p = \mathbf{F}^p. \quad (79)$$

Then, the following incremental form can be computed:

$$\Delta \mathbf{F}_*^p = -\Delta \gamma \mathbf{n}_g - \gamma \Delta \mathbf{n}_g. \quad (80)$$

The expanded version of Eq.(80) is given by

$$\Delta \mathbf{F}_*^p = -\Delta \gamma \mathbf{n}_g - \gamma \frac{\partial \mathbf{n}_g}{\partial \vartheta} \Delta \vartheta - \gamma \frac{\partial \mathbf{n}_g}{\partial \mathbf{F}^e} : \Delta \mathbf{F}^e. \quad (81)$$

The increment of the elastic part of the deformation gradient is given by

$$\Delta \mathbf{F}^e = \Delta \mathbf{F} \mathbf{F}^{p-1} - \Delta \gamma \mathbf{F}^{e,tr} \mathbf{n}_g - \gamma \mathbf{F}^{e,tr} \frac{\partial \mathbf{n}_g}{\partial \vartheta} \Delta \vartheta - \gamma \mathbf{F}^{e,tr} \frac{\partial \mathbf{n}_g}{\partial \mathbf{F}^e} : \Delta \mathbf{F}^e. \quad (82)$$

Reformulating the consistency condition

$$\Delta f = \frac{\partial f}{\partial \mathbf{F}^e} : \Delta \mathbf{F}^e + \frac{\partial f}{\partial \bar{\epsilon}} \Delta \bar{\epsilon} + \frac{\partial f}{\partial \vartheta} \Delta \vartheta = 0. \quad (83)$$

with

$$\Delta\bar{\epsilon} = \sqrt{\frac{2}{3}}\Delta\gamma\|\mathbf{n}_g\| + \sqrt{\frac{2}{3}}\gamma\frac{\partial\|\mathbf{n}_g\|}{\partial\mathbf{F}^e} : \Delta\mathbf{F}^e + \sqrt{\frac{2}{3}}\gamma\frac{\partial\|\mathbf{n}_g\|}{\partial\vartheta}\Delta\vartheta. \quad (84)$$

Therefore, one can express

$$\begin{aligned} \Delta f &= \left( \frac{\partial f}{\partial\bar{\epsilon}}\sqrt{\frac{2}{3}}\|\mathbf{n}_g\| \right) \Delta\gamma + \left( \frac{\partial f}{\partial\bar{\epsilon}}\sqrt{\frac{2}{3}}\gamma\frac{\partial\|\mathbf{n}_g\|}{\partial\vartheta} + \frac{\partial f}{\partial\vartheta} \right) \Delta\vartheta + \\ &\quad \left( \frac{\partial f}{\partial\bar{\epsilon}}\sqrt{\frac{2}{3}}\gamma\frac{\partial\|\mathbf{n}_g\|}{\partial\mathbf{F}^e} + \frac{\partial f}{\partial\mathbf{F}^e} \right) : \Delta\mathbf{F}^e = 0. \end{aligned} \quad (85)$$

From Eq.(85), the increment of the consistency parameter reads:

$$\Delta\gamma = -\underbrace{\frac{\partial f}{\partial\bar{\epsilon}}\sqrt{\frac{2}{3}}\gamma\frac{\partial\|\mathbf{n}_g\|}{\partial\vartheta} + \frac{\partial f}{\partial\vartheta}}_{\frac{\partial\gamma}{\partial\vartheta}}\Delta\vartheta - \underbrace{\frac{\partial f}{\partial\bar{\epsilon}}\sqrt{\frac{2}{3}}\gamma\frac{\partial\|\mathbf{n}_g\|}{\partial\mathbf{F}^e} + \frac{\partial f}{\partial\mathbf{F}^e}}_{\frac{\partial\gamma}{\partial\mathbf{F}^e}} : \Delta\mathbf{F}^e. \quad (86)$$

Accordingly, one can express the increment of  $\Delta\mathbf{F}_*^p$  as follows:

$$\Delta\mathbf{F}_*^p = -\underbrace{\left( \frac{\partial\gamma}{\partial\vartheta}\mathbf{n}_g + \gamma\frac{\partial\mathbf{n}_g}{\partial\vartheta} \right)}_{\mathbf{H}^p}\Delta\vartheta - \underbrace{\left( \mathbf{n}_g \otimes \frac{\partial\gamma}{\partial\mathbf{F}^e} + \gamma\frac{\partial\mathbf{n}_g}{\partial\mathbf{F}^e} \right)}_{\mathbb{H}^p} : \Delta\mathbf{F}^e. \quad (87)$$

Inserting the derivations obtained in Eq.(86) into Eq.(82) yields

$$\Delta\mathbf{F}^e = \mathbb{N}^{*-1} : (\Delta\mathbf{F}\mathbf{F}^{p-1}) - \mathbb{N}^{*-1} : \underbrace{\left( \mathbf{F}^{e,tr}\mathbf{n}_g\frac{\partial\gamma}{\partial\vartheta} + \gamma\mathbf{F}^{e,tr}\frac{\partial\mathbf{n}_g}{\partial\vartheta} \right)}_{\mathbf{T}_{\mathbf{F}^e}}\Delta\vartheta, \quad (88)$$

where

$$\mathbb{N} = \bar{\mathbb{I}} + \gamma\mathbf{F}^{e,tr}\frac{\partial\mathbf{n}_g}{\partial\mathbf{F}^e} \quad \text{with} \quad \mathbb{N}^* = \mathbb{N} + (\mathbf{F}^{e,tr}\mathbf{n}_g) \otimes \frac{\partial\gamma}{\partial\mathbf{F}^e}; \quad \bar{\mathbb{I}} = \bar{\mathbb{I}}_{ijkl} = \delta_{ik}\delta_{jl} \quad (89)$$

In addition, the following increment should be computed:

$$\Delta\bar{\mathbf{S}} = \frac{\partial\bar{\mathbf{S}}}{\partial\vartheta}\Delta\vartheta + \left( \frac{\partial\bar{\mathbf{S}}}{\partial\mathbf{E}^e} : \frac{\partial\mathbf{E}^e}{\partial\mathbf{F}^e} \right) : \Delta\mathbf{F}^e, \quad (90)$$

whereby the elastic thermal constitutive operator,  $\mathbf{C}^{e,th}$ , and the mechanical elastic tangent,  $\mathbb{C}_*^{e,mech}$ , can be defined:

$$\mathbf{C}^{e,th} := \left( \frac{1}{\vartheta_0}(\mathbb{C}_0^e : \mathbf{E}^e) - \frac{c^*}{\vartheta_0}\mathbf{C}^{e-1} \right) \quad (91)$$

$$\mathbb{C}_*^{e,mech} = \left( \underbrace{\left( \frac{\vartheta}{\vartheta_0}\mathbb{C}_0^e + c^*\left(1 - \frac{\vartheta}{\vartheta_0}\right)\frac{\partial\mathbf{C}^{e-1}}{\partial\mathbf{E}^e} \right)}_{\mathbb{C}^{e,mech}} : \frac{\partial\mathbf{E}^e}{\partial\mathbf{F}^e} \right), \quad (92)$$

with

$$\frac{\partial\mathbf{C}^{e-1}}{\partial\mathbf{E}^e} = 2\frac{\partial\mathbf{C}^{e-1}}{\partial\mathbf{C}^e} \Rightarrow \left( \frac{\partial\mathbf{C}^{e-1}}{\partial\mathbf{E}^e} \right)_{ijkl} = -\left( \mathbf{C}_{ik}^{e-1}\mathbf{C}_{jl}^{e-1} + \mathbf{C}_{il}^{e-1}\mathbf{C}_{jk}^{e-1} \right); \quad \frac{\partial\mathbf{E}^e}{\partial\mathbf{F}^e} = \frac{1}{2}\frac{\partial\mathbf{C}^e}{\partial\mathbf{F}^e} = \frac{1}{2}\mathbb{C}^*. \quad (93)$$

In addition to the previous results, the increment of the first Piola-Kirchhoff stress tensor ( $\mathbf{P} := \mathbf{FS}$ ) renders:

$$\Delta\mathbf{P} = \Delta\mathbf{FS} + \mathbf{F}\Delta\mathbf{S} = \Delta\mathbf{F}(\mathbf{F}^{p-1}\bar{\mathbf{S}}\mathbf{F}^{p-T}) + \mathbf{F}\Delta(\mathbf{F}^{p-1}\bar{\mathbf{S}}\mathbf{F}^{p-T}), \quad (94)$$

where

$$\Delta(\mathbf{FS}) = \Delta\mathbf{F}(\mathbf{F}^{p-1}\bar{\mathbf{S}}\mathbf{F}^{p-T}) + \mathbf{F}\Delta\mathbf{F}^{p-1}\bar{\mathbf{S}}\mathbf{F}^{p-T} + \mathbf{FF}^{p-1}\Delta\bar{\mathbf{S}}\mathbf{F}^{p-T} + \mathbf{FF}^{p-1}\bar{\mathbf{S}}\Delta\mathbf{F}^{p-T}, \quad (95)$$

being

$$\Delta\mathbf{F}^{p-T} = \Delta(\mathbf{F}_*^p\mathbf{F}_n^{p-T}) = \Delta\mathbf{F}_*^p\mathbf{F}_n^{p-T}. \quad (96)$$

Note that Eq.(95) can be expressed in expanded form as:

$$\begin{aligned} \Delta(\mathbf{FS}) &= \Delta\mathbf{F}(\mathbf{F}^{p-1}\bar{\mathbf{S}}\mathbf{F}^{p-T}) + \\ &\quad \mathbf{FF}_n^{p-1}(\mathbf{H}^p\Delta\vartheta + \mathbb{H}^p : \Delta\mathbf{F}^e)\bar{\mathbf{S}}\mathbf{F}^{p-T} + \\ &\quad \mathbf{FF}^{p-1}(\mathbf{C}^{e,th}\Delta\vartheta + \mathbb{C}_{*,mech}^{e,mech} : \Delta\mathbf{F}^e)\mathbf{F}^{p-T} + \\ &\quad \mathbf{FF}^{p-1}\bar{\mathbf{S}}(\mathbf{H}^p\Delta\vartheta + \mathbb{H}^p : \Delta\mathbf{F}^e)\mathbf{F}_n^{p-T}. \end{aligned} \quad (97)$$

In condensed format, the increment first Piola-Kirchhoff stress tensor obeys the following expression:

$$\Delta(\mathbf{FS}) = \mathbb{C}^{mech} : \Delta\mathbf{F} + \mathbf{C}^{th}\Delta\vartheta \Rightarrow \Delta(\mathbf{FS})_{ij} = \mathbb{C}_{ijkl}^{mech}\Delta\mathbf{F}_{kl} + \mathbf{C}_{ij}^{th}\Delta\vartheta, \quad (98)$$

where  $\mathbb{C}^{mech}$  and  $\mathbf{C}^{th}$  denote the algorithmic consistent mechanical and thermal tangent moduli, which closed expressions take the form:

$$\begin{aligned} \mathbb{C}^{mech} \Rightarrow \mathbb{C}_{ijkl}^{mech} &= \delta_{ik}\mathbf{F}_{ln}^{p-1}\bar{\mathbf{S}}_{ns}\mathbf{F}_{sj}^{p-T} + \\ &\quad \mathbf{F}_{im}\mathbf{F}_{n,mx}^{p-1}\mathbb{H}_{xnab}^p\mathbb{N}_{abky}^{*-1}\mathbf{F}_{ly}^{p-1}\bar{\mathbf{S}}_{ns}\mathbf{F}_{sj}^{p-T} + \\ &\quad \mathbf{F}_{im}\mathbf{F}_{mn}^{p-1}\mathbb{C}_{*,nsab}^{e,mech}\mathbb{N}_{abky}^{*-1}\mathbf{F}_{ly}^{p-1}\mathbf{F}_{sj}^{p-T} + \\ &\quad \mathbf{F}_{im}\mathbf{F}_{mn}^{p-1}\bar{\mathbf{S}}_{ns}\mathbb{H}_{sxab}^p\mathbb{N}_{abky}^{*-1}\mathbf{F}_{ly}^{p-1}\mathbf{F}_{n,xj}^{p-T}, \end{aligned} \quad (99)$$

$$\begin{aligned} \mathbf{C}^{th} \Rightarrow \mathbf{C}_{ij}^{th} &= \mathbf{F}_{im}\mathbf{F}_{n,mx}^{p-1}\mathbf{H}_{xn}^p\bar{\mathbf{S}}_{ns}\mathbf{F}_{sj}^{p-T} + \\ &\quad \mathbf{F}_{im}\mathbf{F}_{n,mx}^{p-1}\mathbb{H}_{xnab}^p\mathbf{T}_{\mathbf{F}^e,ab}^*\bar{\mathbf{S}}_{ns}\mathbf{F}_{sj}^{p-T} + \\ &\quad \mathbf{F}_{im}\mathbf{F}_{mn}^{p-1}\mathbf{C}_{ns}^{e,th}\mathbf{F}_{sj}^{p-T} + \\ &\quad \mathbf{F}_{im}\mathbf{F}_{mn}^{p-1}\mathbb{C}_{*,nsab}^{e,mech}\mathbf{T}_{\mathbf{F}^e,ab}^*\mathbf{F}_{sj}^{p-T} + \\ &\quad \mathbf{F}_{im}\mathbf{F}_{mn}^{p-1}\bar{\mathbf{S}}_{ns}\mathbf{H}_{sx}^p\mathbf{F}_{n,xj}^{p-T} + \\ &\quad \mathbf{F}_{im}\mathbf{F}_{mn}^{p-1}\bar{\mathbf{S}}_{ns}\mathbb{H}_{sxab}^p\mathbf{T}_{\mathbf{F}^e,ab}^*\mathbf{F}_{n,xj}^{p-T}. \end{aligned} \quad (100)$$

### 3.3. Variational formulation of the coupled thermo-mechanical problem

In the subsequent developments, we briefly review the basics concepts with regard to the IVP (Initial Boundary Value Problem) for coupled thermo-mechanical analysis. The first step towards the derivation concerns the formulation of the linear momentum, energy and entropy variation balance laws for a solid undergoing large strains and thermal variations.

Assuming quasi-static conditions, the local form of the balance of linear momentum in terms of the reference coordinates  $\mathbf{X} \in \mathcal{B}_0$  renders:

$$\text{DIV}[\mathbf{P}] + \mathbf{F}_v = 0 \text{ in } \mathcal{B}_0 \quad (101)$$

where  $\mathbf{F}_v$  denotes body forces per unit of reference volume, and the operator  $\text{DIV}[\bullet]$  stands for the divergence with respect to the reference setting.

The local form of the energy balance in the material description reads

$$\dot{e} = \mathbf{S} : \dot{\mathbf{E}} + R - \text{DIV} [\mathbf{Q}] \text{ in } \mathcal{B}_0, \quad (102)$$

where  $R$  is the internal heat source and  $\mathbf{Q} = J\mathbf{q}\mathbf{F}^{-T}$  denotes the first Piola-Kirchhoff heat flux. Invoking the second law of thermodynamics, see Eq.(22), we end up with the evolution equation of the temperature, which renders

$$\vartheta\dot{\eta^e} = \mathcal{D}_{\text{int}}^{\text{mech}} - \text{DIV} [\mathbf{Q}] + R. \quad (103)$$

Defining  $\vartheta\dot{\eta^e} = c_p\dot{\vartheta} + \mathcal{H}$ , Eq.(103) can be recast into

$$c_p\dot{\vartheta} = \mathcal{D}_{\text{int}}^{\text{mech}} - \text{DIV} [\mathbf{Q}] + R - \mathcal{H}, \quad (104)$$

where  $\mathcal{H}$  stands for structural heating or cooling and is given by:  $\mathcal{H} = -\vartheta\frac{\partial^2\psi^e}{\partial\vartheta\partial\mathbf{E}} : \dot{\mathbf{E}}$

### 3.4. Weak formulation and consistent linearization

This section briefly outlines the construction of the weak form of the coupled thermo-mechanical IBVP which is governed by the balance of linear momentum, Eq.(101), and the energy balance equation in entropy form, Eq.(104). The weak forms of both balance equations represent the most convenient setting to formulate the corresponding numerical approximation based on the Finite Element Method (FEM), which is constructed by means of the standard Galerkin procedure.

Lets assume that the reference body boundary  $\partial\mathcal{B}_0$  is subdivided into the disjointed parts  $\partial\mathcal{B}_{0,u} \subset \partial\mathcal{B}_0$  and  $\partial\mathcal{B}_{0,t} \subset \partial\mathcal{B}_0$ , with  $\partial\mathcal{B}_0 = \partial\mathcal{B}_{0,u} \cup \partial\mathcal{B}_{0,t}$  and  $\partial\mathcal{B}_{0,u} \cap \partial\mathcal{B}_{0,t} = \emptyset$  corresponding to the mechanical subproblem and  $\partial\mathcal{B}_{0,\vartheta} \subset \partial\mathcal{B}_0$  and  $\partial\mathcal{B}_{0,q} \subset \partial\mathcal{B}_0$ , with  $\partial\mathcal{B}_0 = \partial\mathcal{B}_{0,\vartheta} \cup \partial\mathcal{B}_{0,q}$  and  $\partial\mathcal{B}_{0,\vartheta} \cap \partial\mathcal{B}_{0,q} = \emptyset$  corresponding to the thermal sub-problem. As customary, appropriate boundary conditions must be defined in order to guarantee the well-posedness of the thermo-mechanical IBVP.

With regard to the energy balance, the corresponding weak form reads

$$G^\vartheta(\mathbf{u}, \vartheta, \delta\vartheta) = \int_{\mathcal{B}_0} \left( \mathcal{D}_{\text{int}}^{\text{mech}} - \text{DIV} [\mathbf{Q}] + R - \mathcal{H} - c_p\dot{\vartheta} \right) \delta\vartheta dV = 0, \quad (105)$$

where  $\delta\vartheta$  renders the virtual temperature. Invoking the Divergence Theorem

$$\int_{\mathcal{B}_0} \text{DIV} [\mathbf{Q}] \delta\vartheta dV = \int_{\partial\mathcal{B}_0} \mathbf{Q}\mathbf{N} \delta\vartheta dA - \int_{\mathcal{B}_0} \mathbf{Q}\nabla_{\mathbf{X}}\delta\vartheta dV, \quad (106)$$

with  $\nabla_{\mathbf{X}}\delta\vartheta$  denoting the material gradient of the virtual temperature, one obtains the following weak form for the energy balance:

$$G^\vartheta(\mathbf{u}, \vartheta, \delta\vartheta) = \int_{\mathcal{B}_0} \mathcal{D}_{\text{int}}^{\text{mech}} \delta\vartheta dV + \int_{\mathcal{B}_0} R \delta\vartheta dV - \int_{\mathcal{B}_0} \mathcal{H} \delta\vartheta dV - \int_{\mathcal{B}_0} c_p\dot{\vartheta} \delta\vartheta dV + \int_{\mathcal{B}_0} J\mathbf{q}\nabla_{\mathbf{X}}\delta\vartheta dV - \int_{\partial\mathcal{B}_0} h_Q \delta\vartheta dA = 0 \quad (107)$$

where  $h_Q = \mathbf{Q}\mathbf{N}$  represents the surface heat flux and  $\mathbf{N}$  denotes the reference outer normal vector. Note that  $\nabla_{\mathbf{X}}\delta\vartheta = \mathbf{F}^{-T}\nabla_{\mathbf{X}}\delta\vartheta$ .

An analogous procedure can be performed for the linear momentum balance equation:

$$G^u(\mathbf{u}, \vartheta, \delta\mathbf{u}) = \int_{\mathcal{B}_0} \mathbf{P} : \nabla_{\mathbf{X}}\delta\mathbf{u} dV - \int_{\partial\mathcal{B}_0} \delta\mathbf{u}(\mathbf{P}\mathbf{N}) dA - \int_{\mathcal{B}_0} \mathbf{F}_v \delta\mathbf{u} dV \quad (108)$$

where  $\delta\mathbf{u}$  renders the virtual displacement and  $\delta\mathbf{F} = \nabla_{\mathbf{X}}\delta\mathbf{u}$  and  $\mathbf{T} = \mathbf{P}\mathbf{N}$  denotes the First Piola-Kirchhoff traction vector. As customary, the invocation of the Gauss-Green Theorem is performed for the derivation of the weak form given in Eq.(108).

The standard FE approach is employed for the interpolation of the actual, virtual and incremental displacement and thermal fields. This interpolation reads

$$\mathbf{u} \approx \mathbf{u}^h = \sum_{A=1}^n N^A \mathbf{d}_A = \mathbf{N}\mathbf{d}; \quad \delta\mathbf{u} \approx \delta\mathbf{u}^h = \sum_{A=1}^n N^A \delta\mathbf{d}_A = \mathbf{N}\delta\mathbf{d}; \quad \Delta\mathbf{u} \approx \Delta\mathbf{u}^h = \sum_{A=1}^n N^A \Delta\mathbf{d}_A = \mathbf{N}\Delta\mathbf{d} \quad (109)$$

$$\vartheta \approx \sum_{A=1}^n N^A \hat{\vartheta}_A = \hat{\mathbf{N}} \hat{\boldsymbol{\vartheta}}, \quad \delta\vartheta \approx \sum_{A=1}^n N^A \delta\hat{\vartheta}_A = \hat{\mathbf{N}} \delta\hat{\boldsymbol{\vartheta}}, \quad \Delta\vartheta \approx \sum_{A=1}^n N^A \Delta\hat{\vartheta}_A = \hat{\mathbf{N}} \Delta\hat{\boldsymbol{\vartheta}}, \quad (110)$$

where  $n$  identifies the node number at the element level;  $N^A(\xi)$  stands for the shape functions with  $\xi := \{\xi^1, \xi^2, \xi^3\}$  being the natural coordinates of the isoparametric domain  $\mathcal{A} := \{\xi \in \mathbb{R}^3 \mid -1 \leq \xi^i \leq +1; i = 1, 2, 3\}$ . The insertion of Eqs.(109)–(110) into Eqs.(107)–(108) leads to the discrete version of the variational formulation, which correspond to the form of the element residual vectors.

With regard to the use of a Newton-type solution procedure, the consistent linearization of Eqs.(107)–(108) is carried out by means of the directional derivative concept [26]:

$$\hat{L}[G^\vartheta](\mathbf{d}, \Delta\mathbf{d}, \hat{\boldsymbol{\vartheta}}, \delta\hat{\boldsymbol{\vartheta}}, \Delta\hat{\boldsymbol{\vartheta}}) = G^\vartheta(\mathbf{d}, \hat{\boldsymbol{\vartheta}}, \delta\hat{\boldsymbol{\vartheta}}) + \Delta_{\mathbf{d}} G^\vartheta(\mathbf{d}, \Delta\mathbf{d}, \hat{\boldsymbol{\vartheta}}, \delta\hat{\boldsymbol{\vartheta}}) \Delta\mathbf{d} + \Delta_{\hat{\boldsymbol{\vartheta}}} G^\vartheta(\mathbf{d}, \hat{\boldsymbol{\vartheta}}, \delta\hat{\boldsymbol{\vartheta}}, \Delta\hat{\boldsymbol{\vartheta}}) \Delta\hat{\boldsymbol{\vartheta}} \quad (111)$$

$$\hat{L}[G^u](\mathbf{d}, \delta\mathbf{d}, \Delta\mathbf{d}, \hat{\boldsymbol{\vartheta}}, \Delta\hat{\boldsymbol{\vartheta}}) = G^u(\mathbf{d}, \delta\mathbf{d}, \hat{\boldsymbol{\vartheta}}) + \Delta_{\mathbf{d}} G^u(\mathbf{d}, \delta\mathbf{d}, \Delta\mathbf{d}, \hat{\boldsymbol{\vartheta}}) \Delta\mathbf{d} + \Delta_{\hat{\boldsymbol{\vartheta}}} G^u(\mathbf{d}, \delta\mathbf{d}, \hat{\boldsymbol{\vartheta}}, \Delta\hat{\boldsymbol{\vartheta}}) \Delta\hat{\boldsymbol{\vartheta}}, \quad (112)$$

where  $\Delta_*[\bullet]$  identifies the directional derivative operator with respect to the field  $*$ . This procedure yields to a fully coupled thermo-mechanical system [10], where the element tangent matrices are consistently derived. For both the mechanical and the thermal fields, we assume the identical finite element discretization, which makes the algorithmic implementation very convenient at the element level. It is worth mentioning that standard first-order isoparametric finite elements are used for the mesh of the mechanical and thermal fields. Alternative formulations such as mixed- or enhanced-type finite element technologies can be used without any remarkable limitation [40].

Accordingly, in Eq.(107), the contribution of the structural heating is usually neglected ( $\mathcal{H} \cong 0$ ). Finally, the internal mechanical dissipation  $\mathcal{D}_{\text{int}}^{\text{mech}}$  and the term  $J\mathbf{q}\nabla_{\mathbf{x}}\delta\vartheta$  should be linearized. This procedure is presented in Appendix B.

#### 4. Representative applications

The constitutive formulation previously described is implemented into the commercial FE code ABAQUS by means of user-defined capabilities. The goal of this section is to asses the performance of the proposed formulation. The applications discussed in the sequel are: (i) a verification and validation example regarding dog-bone specimen-types with different material orientations at different temperatures (Section 4.1), and (ii) a structural application involving a three-dimensional 3-point bending example (Section 4.2). Results from both applications are correlated with experimental data taken from available literature. The FE simulations herein presented are carried out using first-order reduced integration solid elements for finite strains. In particular, in order to preclude the well-known transverse shear locking effects, the 3-point bending geometry is discretized using 6 elements over the thickness.

##### 4.1. Model verification and validation: dog-bone specimens

The first application concerns dog-bone specimens subjected to uniform tensile loading with different material orientations with respect to the loading direction. The objective of this first example is the verification and validation of the current formulation for its subsequent application in more complex structural examples. The specimen is manufactured using the short fibre reinforced thermoplastic PA66GF-35, whose material properties are reported in Tables 1 and 2. These properties lie within the specified ranges of the corresponding ISO norms. The fiber distribution was considered to be homogeneous over the cross section of the specimen through the averaging procedure aforementioned. The yielding parameters,  $\zeta_i$ , at room temperature and  $T = 130^\circ \text{ C}$  are given in Tables 3 and 4, respectively, whereas the plastic potential parameters  $\iota_i$  are detailed in Table 5. The characterization of the yield surface for PA66GF-35 is depicted in Figure 6, whereby its adequate convex form can be observed.

The geometry of the specimen is shown in Figure 7.a, where the zero-degree reference direction which is aligned with the loading orientation, is identified. The experimental investigation characterizing these specimens was carried out by de Monte et al. [12]. A previous investigation with regard to the assessment of the geometrically linear version of the current invariant-based thermo-plastic model was performed by the

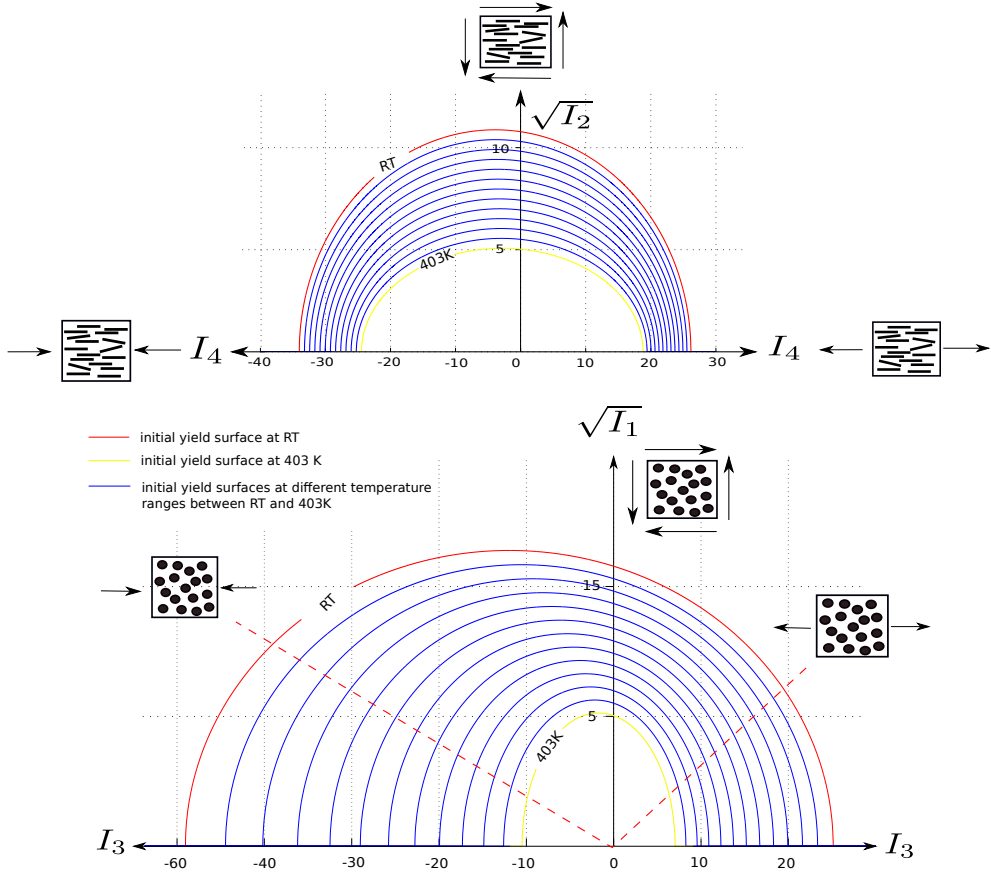


Figure 6: PA66GF-35: characterization of the yield surface.

authors in [10], whereby an excellent correlation with respect to the experimental data was achieved. The variation of the yield locus with temperature is shown in Figure 6, conforming the convex character of this surface.

In the current case, a different FE discretization is employed, which consists of 5680 element. The boundary conditions imposed onto the model replicated those described in [10]: (i) restrained displacements at the clamped edge, and (ii) constrained displacements at the loaded edge except the prescribed displacement along the  $0^\circ$ -direction.

Figures 7.b and 7.c report the experimental–numerical correlation of the monotonic tensile tests under consideration at different temperatures. In these graphs, an excellent agreement between the experimental data and the numerical predictions can be observed. Indeed, a better correlation than that corresponding to the geometrically linear thermo-plastic model [10] is obtained, especially for the case where the preferential fibre orientation forms  $45^\circ$  with the loading direction. This particular case is the configuration where fibers suffer from a more notable rotation along the test, which has been satisfactorily captured using the finite strain model herein developed. The proposed formulation captures the softer behavior at higher temperatures in comparison with the performance at room temperature.

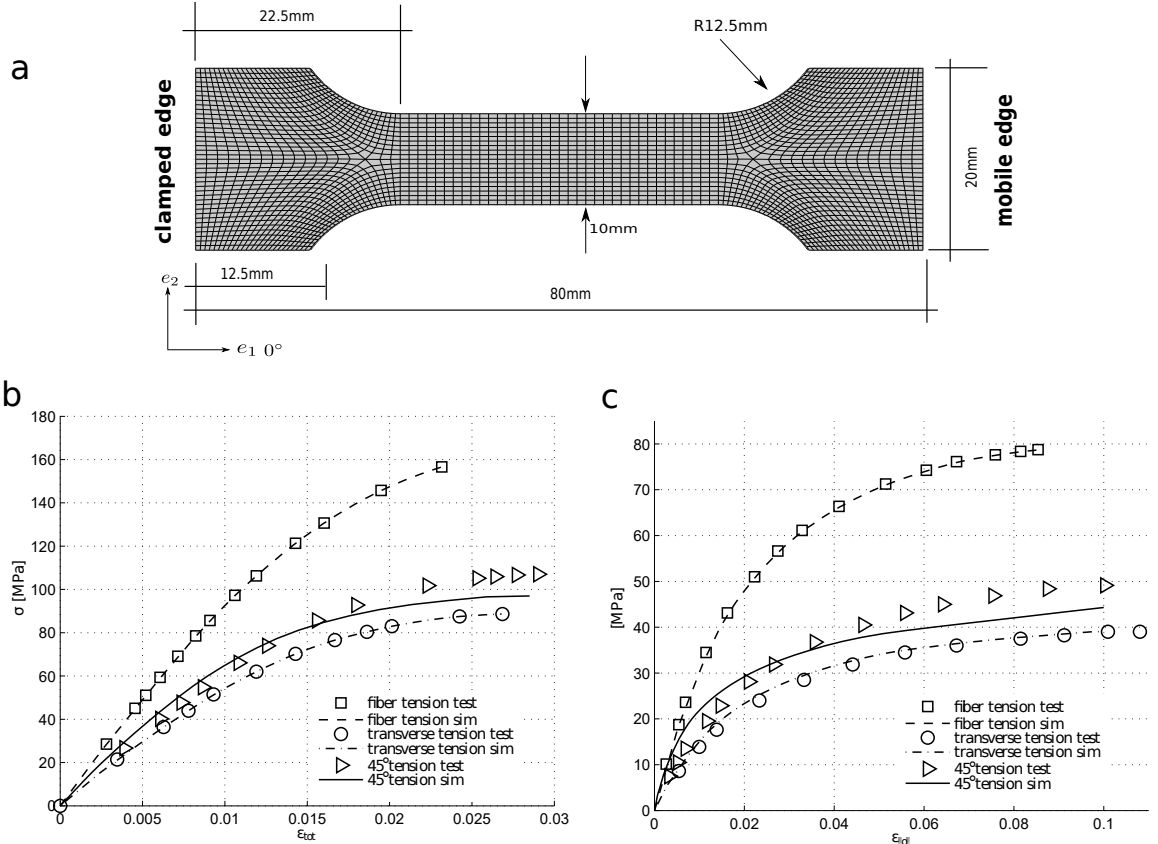


Figure 7: Dog-bone specimens PA66GF-35 under thermo-mechanical uniaxial loading conditions. (a) Specimen definition. (b) Experimental-numerical correlation at room temperature for different preferential fiber orientations. (c) Experimental numerical correlation at  $T = 403$  K for different preferential fiber orientations.

$E_{11}$ (MPa)	$E_{22}$ (MPa)	$G_{12}$ (MPa)	$\nu_{12}$	$\nu_{23}$
9919.13	5270.13	2415.49	0.4	0.61

Table 1: PA66GF-35: mechanical properties.

$c_p$ (J/kg K)	$Z_{11}$ (m/mK)	$Z_{22}$ (m/mK)	$Z_{33}$ (m/mK)	$K_{11}$ (W/mK)	$K_{22}$ (W/mK)	$K_{33}$ (W/mK)
1380	$25 \cdot 10^{-6}$	$28 \cdot 10^{-6}$	$28 \cdot 10^{-6}$	0.67	0.67	0.67

Table 2: PA66GF-35: thermal properties.

$\zeta_1$	$\zeta_2$	$\zeta_3$	$\zeta_4$	$\zeta_5$	$\zeta_6$
$2.648 \times 10^{-4}$	$2.648 \times 10^{-4}$	$3.272 \times 10^{-3}$	$2.523 \times 10^{-5}$	$1.338 \times 10^{-3}$	$2.588 \times 10^{-4}$

Table 3: PA66GF-35: yielding parameters  $\zeta_i$  at room temperature.

#### 4.2. Structural application: 3-point bending test

We now consider a 3-point bending test of a SFRP plate manufactured from PA6GF-30. This application was considered in [44] for different loading velocities. In this investigation, we only consider loading velocity of 1.0 m/s due to the quasi-static character of the developed model. In addition, note that the experimental

$\zeta_1$	$\zeta_2$	$\zeta_3$	$\zeta_4$	$\zeta_5$	$\zeta_6$
$1.409 \times 10^{-3}$	$1.409 \times 10^{-3}$	$7.355 \times 10^{-3}$	$1.224 \times 10^{-4}$	$2.886 \times 10^{-3}$	$1.203 \times 10^{-4}$

Table 4: PA66GF-35: yielding parameters  $\zeta_i$  at  $T = 130^\circ$  C.

$\iota_1$	$\iota_2$
0.001673	-0.000673

Table 5: PA66GF-35: plastic potential parameters  $\iota_i$ .

results reported in [44] correspond to room temperature tests, therefore the lack of the experimental data leads to performing a parametric investigation at different temperatures. The material properties according to [44] (referred as conditioning material) are given in Tables 6, whereas the thermal properties and the plastic data are reported in Tables 7–9, respectively.

$E_{11}$ (MPa)	$E_{22}$ (MPa)	$G_{12}$ (MPa)	$\nu_{12}$	$\nu_{23}$
5211.43	2262.86	1601.7	0.39	0.6

Table 6: PA6GF-30: Mechanical properties.

$c_p$ (J/kg K)	$Z_{11}$ (m/mK)	$Z_{22}$ (m/mK)	$Z_{33}$ (m/mK)	$K_{11}$ (W/mK)	$K_{22}$ (W/mK)	$K_{33}$ (W/mK)
1380	$27 \cdot 10^{-6}$	$28 \cdot 10^{-6}$	$28 \cdot 10^{-6}$	0.23	0.23	0.23

Table 7: PA6GF-30: Thermal properties.

$\zeta_1$	$\zeta_2$	$\zeta_3$	$\zeta_4$	$\zeta_5$	$\zeta_6$
$4.521 \times 10^{-4}$	$4.521 \times 10^{-4}$	$6.624 \times 10^{-3}$	$9.429 \times 10^{-5}$	$3.899 \times 10^{-3}$	$2.196 \times 10^{-4}$

Table 8: PA6GF-30: yielding parameters  $\zeta_i$  at room temperature.

$\iota_1$	$\iota_2$
0.001673	-0.000673

Table 9: PA6GF-30: plastic potential parameters  $\iota_i$  at room temperature.

The geometric description of the test is given in Figure 8.a. The dimensions of the SFRP plate are: (i) length  $L = 50$  mm, (ii) width  $B = 5$  mm, and (iii) thickness  $t = 2$  mm. In line with the previous applications (Section 4.1), uniform material properties over the plate thickness are considered. Preferential fibre orientation is aligned with the axial direction of the specimen. The numerical model consists of the discretization of the SFRP plate using 7200 elements, whereas the pin for the loading application is also meshed using 2100 elements. The external loading is applied through a prescribed vertical displacement downwards at the central pin equal to 9 mm, see Figures 8.a and 8.b. The simulations are conducted using 1000 equal pseudo-time increments. In each increment the coupled global solution scheme is employed. Figure 8.b shows the stress distribution due to the prescribed thermo-mechanical loading, where, as expected, a non uniform strain distribution over the plate thickness is estimated.

Figure 8.c depicts the preferential material orientation predicted by the current models at intermediate stages of the simulation. In this graph, a significant variation of the preferential material direction throughout the process is estimated. This fact stems from the large deformation experienced for the plate, which can notably affect the performance in service and cannot be captured using a geometrically linear model. This becomes evident in the current example and highlights the necessity of triggering the evolution of the

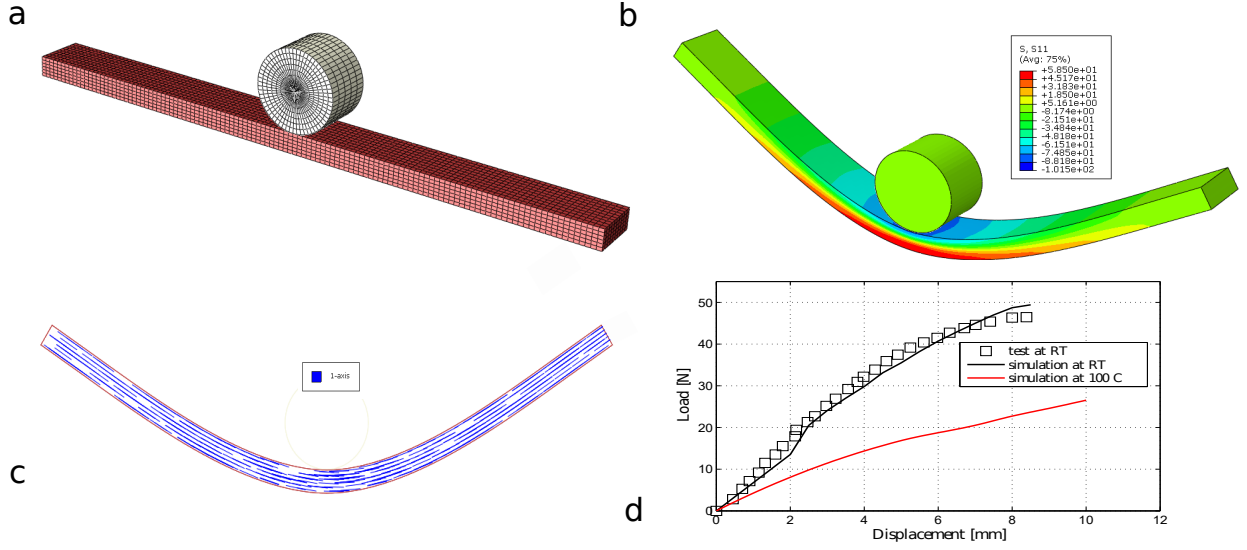


Figure 8: 3-point bending test of PA6GF-30. (a) Specimen definition. (b) Stress distribution at  $T = 100^\circ\text{C}$ . (c) Mapping of the preferential material direction after the computation. (d) Experimental–numerical correlation at room temperature.

preferential material orientation along the deformation process. This issue can be only performed using a geometrically nonlinear setting, complementing the formulation previously developed in [11].

Finally, Figure 8.d depicts the load–central displacement evolution curve of the test at room temperature. In this graph, an initial linear evolution followed by notable nonlinear effects is observed. Regarding the experimental-numerical correlation, this plot shows an excellent agreement between both data. The numerical investigation is extended for a temperature  $T = 100^\circ\text{C}$ . In this graph, it can be observed that a softer response is predicted for this higher temperature. In addition, it is worth mentioning that the current model estimates a smoother transition between the initial linear range and the subsequent nonlinear evolution for  $T = 100^\circ\text{C}$ . This behaviour is fully consistent with the previous data herein reported, allowing to conduct preliminary qualitative simulations with regard to the current application.

## 5. Conclusions

In this investigation, a formulation for invariant-based anisotropic thermo-plasticity at large deformations including aspects of its numerical treatment within the FE framework has been presented.

The proposed formulation assumed a non-associate flow rule for triggering the inelastic evolution, in which a multiplicative decomposition of the deformation gradient has been envisaged. The theoretical development strictly complied with the thermodynamic restrictions and has been characterized by the introduction of a novel invariant set for the characterization of the yield and the plastic potential surfaces.

On the computational side, the main aspects of its finite element implementation have been addressed. Special attention was devoted to the numerical treatment of the return-mapping elasto-plastic algorithm, whereby a closed form for the algorithmic consistent thermo-mechanical tangent moduli has been obtained.

Finally, the performance of the current model has been validated through several monotonic tensile tests with different temperatures and preferential material orientations. Subsequently, the model has been incorporated into the simulation of a 3-point bending test. One key aspect regarded the possibility of triggering the preferential material orientation along the deformation process, which provided very accurate predictions with respect to the experimental trends herein analyzed. The excellent experimental–numerical correlation corresponding to these examples demonstrated the applicability of the developed formulation.

## Acknowledgments

The authors are thankful to Dr.-Ing. Benedikt Daum for many helpful comments and discussions. RR, SS and AD gratefully acknowledge the financial support of the German Research Council (DFG) through the program SPP 1640 (joining by plastic deformation) under the contract No. RO 706/6-2. JR acknowledges the support of the Spanish Ministry of Economy and Competitiveness/FEDER (DPI2012-37187) and the Andalusian Government (Projects of Excellence No. TEP-7093 and P12-TEP-1050). AD gratefully acknowledges the support of Mr. and Mrs. Dean.

## Appendix A. Derivatives of the residual equations in the plastic corrector step

This appendix outlines the required derivations corresponding to the local Newton-Raphson IVBP given in Eq.(76) (Section 3.1).

We start the derivation computing the increment of  $\mathbf{F}^e = \mathbf{F}^{e,tr} (\mathbf{1} - \gamma \mathbf{n}_g)$ , which reads:

$$\Delta \mathbf{F}^e = \mathbf{F}^{e,tr} \left( -\Delta \gamma \mathbf{n}_g - \gamma \frac{\partial \mathbf{n}_g}{\partial \mathbf{F}^e} : \Delta \mathbf{F}^e - \gamma \cancel{\frac{\partial \mathbf{n}_g}{\partial \bar{\epsilon}}}^0 \Delta \bar{\epsilon} - \gamma \cancel{\frac{\partial \mathbf{n}_g}{\partial \eta^p}}^0 \Delta \eta^p \right), \quad (\text{A.1})$$

then, the entries of the first row of  $\mathbf{J}$  read:

$$\frac{\partial \mathbf{R}_{\mathbf{F}^e}}{\partial \mathbf{F}^e} = \mathbb{V}^*, \quad (\text{A.2})$$

with

$$\mathbb{V}^* \Rightarrow \mathbb{V}_{ijkl}^* = \left( \delta_{ik} \delta_{jl} + \gamma \mathbf{F}_{im}^{e,tr} \frac{\partial \mathbf{n}_{g,mj}}{\mathbf{F}_{kl}^e} \right). \quad (\text{A.3})$$

and

$$\frac{\partial \mathbf{R}_{\mathbf{F}^e}}{\partial \bar{\epsilon}} = 0; \quad \frac{\partial \mathbf{R}_{\mathbf{F}^e}}{\partial \eta^p} = 0; \quad \frac{\partial \mathbf{R}_{\mathbf{F}^e}}{\partial \gamma} = \mathbf{F}^{e,tr} \mathbf{n}_g. \quad (\text{A.4})$$

Analogously, one can compute:

$$\Delta \bar{\epsilon} = \sqrt{\frac{2}{3}} \Delta \gamma \|\mathbf{n}_g\| + \sqrt{\frac{2}{3}} \gamma \frac{\partial \|\mathbf{n}_g\|}{\partial \mathbf{F}^e} : \Delta \mathbf{F}^e + \sqrt{\frac{2}{3}} \gamma \cancel{\frac{\partial \|\mathbf{n}_g\|}{\partial \eta^p}}^0 \Delta \eta^p. \quad (\text{A.5})$$

Exploiting Eq.(A.5), the first entry of the second row of  $\mathbf{J}$  takes the form:

$$\frac{\partial \mathbf{R}_{\bar{\epsilon}}}{\partial \mathbf{F}^e} = -\sqrt{\frac{2}{3}} \gamma \frac{\partial \|\mathbf{n}_g\|}{\partial \mathbf{F}^e}, \quad (\text{A.6})$$

with

$$\frac{\partial \|\mathbf{n}_g\|}{\partial \mathbf{F}^e} = \frac{\mathbf{n}_g}{\|\mathbf{n}_g\|} : \frac{\partial \mathbf{n}_g}{\partial \mathbf{F}^e}. \quad (\text{A.7})$$

Note that since  $\mathbf{n}_g = \mathbb{M} : \bar{\Sigma}_s$ , one finds

$$\frac{\partial \mathbf{n}_g}{\partial \mathbf{F}^e} = \mathbb{M} : \frac{\partial \bar{\Sigma}_s}{\partial \mathbf{F}^e} \Rightarrow \left( \frac{\partial \mathbf{n}_g}{\partial \mathbf{F}^e} \right)_{ijkl} = \mathbb{M}_{ijab} \left( \frac{\partial \bar{\Sigma}_s}{\partial \mathbf{F}^e} \right)_{abkl}, \quad (\text{A.8})$$

where

$$\begin{aligned} \frac{\partial \bar{\Sigma}_s}{\partial \mathbf{F}^e} &= \frac{1}{2} \frac{\partial (\bar{\Sigma} + \bar{\Sigma}^T)}{\partial \mathbf{F}^e} \Rightarrow \left( \frac{\partial \bar{\Sigma}_s}{\partial \mathbf{F}^e} \right)_{ijkl} = \frac{1}{2} \mathbb{C}_{imkl}^* \bar{\mathbf{S}}_{mj} + \frac{1}{2} \mathbb{C}_{mkl}^* \bar{\mathbf{S}}_{im} + \\ &\quad \frac{1}{4} \mathbf{C}_{im}^e \mathbb{C}_{mjab}^{e,mech} \mathbb{C}_{abkl}^* + \frac{1}{4} \mathbf{C}_{mj}^e \mathbb{C}_{imab}^{e,mech} \mathbb{C}_{abkl}^*, \end{aligned} \quad (\text{A.9})$$

where

$$\mathbb{C}^* \Rightarrow \mathbb{C}_{ijkl}^* = \left( \frac{\partial \mathbf{C}^e}{\partial \mathbf{F}^e} \right)_{ijkl} = \delta_{il} \mathbf{F}_{kj}^e + \delta_{jl} \mathbf{F}_{ki}^e. \quad (\text{A.10})$$

The remaining entries of the second row of  $\mathbf{J}$  render:

$$\frac{\partial R_{\bar{\epsilon}}}{\partial \bar{\epsilon}} = 1; \quad \frac{\partial R_{\bar{\epsilon}}}{\partial \eta^p} = 0; \quad \frac{\partial R_{\bar{\epsilon}}}{\partial \gamma} = -\sqrt{\frac{2}{3}} \|\mathbf{n}_g\|. \quad (\text{A.11})$$

The increment of the plastic entropy reads:

$$\Delta \eta^p = \Delta \gamma g_\vartheta + \gamma (\mathbb{M}_\vartheta : \bar{\Sigma}_s) : \frac{\partial \bar{\Sigma}_s}{\partial \mathbf{F}^e} \overset{0}{\nearrow} \Delta \mathbf{F}^e + \gamma \frac{\partial g_\vartheta}{\partial \bar{\epsilon}} \Delta \bar{\epsilon}. \quad (\text{A.12})$$

Appropriately, the entries of the third row of  $\mathbf{J}$  reads the following

$$\frac{\partial R_{\eta^p}}{\partial \mathbf{F}^e} = -\gamma (\mathbb{M}_\vartheta : \bar{\Sigma}_s) : \frac{\partial \bar{\Sigma}_s}{\partial \mathbf{F}^e}, \quad \frac{\partial R_{\eta^p}}{\partial \bar{\epsilon}} = 0; \quad \frac{\partial R_{\eta^p}}{\partial \eta^p} = 1; \quad \frac{\partial R_{\eta^p}}{\partial \gamma} = -\Delta \gamma g_\vartheta. \quad (\text{A.13})$$

Finally, the incremental form of the yield function is given by

$$\Delta f = \frac{\partial f}{\partial \mathbf{F}^e} : \Delta \mathbf{F}^e + \frac{\partial f}{\partial \bar{\epsilon}} \Delta \bar{\epsilon} + \frac{\partial f}{\partial \eta^p} \Delta \eta^p + \frac{\partial f}{\partial \gamma} \Delta \gamma = 0. \quad (\text{A.14})$$

Therefore, the entries of the fourth row of  $\mathbf{J}$  can be expressed as:

$$\frac{\partial f}{\partial \mathbf{F}^e} = (\mathbb{K} : \bar{\Sigma}_s + \mathbf{L}) : \frac{\partial \bar{\Sigma}_s}{\partial \mathbf{F}^e}; \quad \frac{\partial f}{\partial \bar{\epsilon}} = \frac{1}{2} \bar{\Sigma}_s : \frac{\partial \mathbb{K}}{\partial \bar{\epsilon}} : \bar{\Sigma}_s + \frac{\partial \mathbf{L}}{\partial \bar{\epsilon}} : \bar{\Sigma}_s; \quad \frac{\partial f}{\partial \eta^p} = 0; \quad \frac{\partial f}{\partial \gamma} = 0. \quad (\text{A.15})$$

## Appendix B. Linearization of the internal dissipation and the heat flux

This Appendix presents the details with regard to the linearization of the internal dissipation and the heat flux terms, see Section 3.4.

With regard to the internal dissipation, recalling Eq.(31) and neglecting the negligible hardening contribution  $\dot{\psi}^p$ , one obtains

$$\mathcal{D}_{\text{int}}^{\text{mech}} = \bar{\Sigma}_s : \mathbf{L}^p = \dot{\gamma} \bar{\Sigma}_s : \mathbf{n}_g = \dot{\gamma} \bar{\Sigma}_s : \mathbb{M} : \bar{\Sigma}_s = \frac{1}{\Delta t} \gamma \bar{\Sigma}_s : \mathbb{M} : \bar{\Sigma}_s = \frac{2}{\Delta t} \gamma g, \quad (\text{B.1})$$

therefore its increment renders:

$$\Delta \mathcal{D}_{\text{int}}^{\text{mech}} = \frac{2}{\Delta t} \Delta \gamma g + \frac{2}{\Delta t} \gamma \Delta g, \quad (\text{B.2})$$

where

$$\Delta g = \bar{\Sigma}_s : \mathbb{M} : \Delta \bar{\Sigma}_s + \frac{1}{2} \bar{\Sigma}_s : \Delta \mathbb{M} : \bar{\Sigma}_s = \mathbf{n}_g : \Delta \bar{\Sigma}_s + g_\vartheta \Delta \vartheta. \quad (\text{B.3})$$

Substituting the given definition of  $\Delta \gamma$  and  $\Delta \bar{\Sigma}_s$ , one obtains

$$\Delta \mathcal{D}_{\text{int}}^{\text{mech}} = \frac{2}{\Delta t} \left( \frac{\partial \gamma}{\partial \vartheta} \Delta \vartheta + \frac{\partial \gamma}{\partial \mathbf{F}^e} : \Delta \mathbf{F}^e \right) g + \frac{2}{\Delta t} \gamma \left( \mathbf{n}_g : \left( \frac{\partial \bar{\Sigma}_s}{\partial \vartheta} \Delta \vartheta + \frac{\partial \bar{\Sigma}_s}{\partial \mathbf{F}^e} : \Delta \mathbf{F}^e \right) + g_\vartheta \Delta \vartheta \right). \quad (\text{B.4})$$

After some manipulations,  $\Delta \mathcal{D}_{\text{int}}^{\text{mech}}$  can be expressed as

$$\Delta \mathcal{D}_{\text{int}}^{\text{mech}} = l^{\mathcal{D}} \Delta \vartheta + \mathbf{L}^{\mathcal{D}} : \Delta \mathbf{F}^e. \quad (\text{B.5})$$

Subsequently, the insertion of the definition of  $\Delta\mathbf{F}^e$  renders

$$\Delta\mathcal{D}_{\text{int}}^{\text{mech}} = l^{\mathcal{D}} \Delta\vartheta + \mathbf{L}^{\mathcal{D}} : (\mathbb{N}^{*-1} : (\Delta\mathbf{F}\mathbf{F}^{p-1}) + \mathbf{T}_{\mathbf{F}^e}^* \Delta\vartheta) = (l^{\mathcal{D}} + \mathbf{L}^{\mathcal{D}} : \mathbf{T}_{\mathbf{F}^e}^*) \Delta\vartheta + \mathbf{L}^{\mathcal{D}} : (\mathbb{N}^{*-1} : (\Delta\mathbf{F}\mathbf{F}^{p-1})), \quad (\text{B.6})$$

where

$$\Delta\mathcal{D}_{\text{int}}^{\text{mech}} = \underbrace{(l^{\mathcal{D}} + \mathbf{L}_{ij}^{\mathcal{D}} : \mathbf{T}_{\mathbf{F}^e,ij}^*) \Delta\vartheta}_{\frac{\partial\mathcal{D}_{\text{int}}^{\text{mech}}}{\partial\vartheta}} + \underbrace{\left( \mathbf{L}_{ij}^{\mathcal{D}} \mathbb{N}_{ijkb}^{*-1} \mathbf{F}_{lb}^{p-1} \right) \Delta\mathbf{F}_{kl}}_{\left( \frac{\partial\mathcal{D}_{\text{int}}^{\text{mech}}}{\partial\mathbf{F}} \right)_{kl}}. \quad (\text{B.7})$$

Finally, it remains to linearize the term  $\mathcal{I} = J\mathbf{q}\nabla_{\mathbf{x}}\delta\vartheta$  associated with the heat flux. Invoking the given Duhamels's law of heat conduction, one can express

$$\mathcal{I} = (-\mathbf{k}\nabla_{\mathbf{x}}\vartheta) J\nabla_{\mathbf{x}}\delta\vartheta = -J(\mathbf{k}\nabla_{\mathbf{x}}\vartheta)\nabla_{\mathbf{x}}\delta\vartheta = -J(\mathbf{k}\nabla_{\mathbf{x}}\vartheta\mathbf{F}^{-1})\nabla_{\mathbf{x}}\delta\vartheta\mathbf{F}^{-1}, \quad (\text{B.8})$$

therefor  $\Delta\mathcal{I}$  reads

$$\Delta\mathcal{I} = \mathcal{I}_J + \mathcal{I}_{\vartheta} + \mathcal{I}_{\mathbf{F}}, \quad (\text{B.9})$$

where

$$\mathcal{I}_J = -(\mathbf{k}\nabla_{\mathbf{x}}\vartheta)\nabla_{\mathbf{x}}\delta\vartheta\Delta J = -(\mathbf{k}\nabla_{\mathbf{x}}\vartheta)\nabla_{\mathbf{x}}\delta\vartheta(J\mathbf{F}^{-T} : \Delta\mathbf{F}), \quad (\text{B.10})$$

$$\mathcal{I}_{\vartheta} = -J(\mathbf{k}\nabla_{\mathbf{x}}\Delta\vartheta)\nabla_{\mathbf{x}}\delta\vartheta, \quad (\text{B.11})$$

$$\begin{aligned} \mathcal{I}_{\mathbf{F}} &= -J(\mathbf{k}(\nabla_{\mathbf{x}}\vartheta(-\mathbf{F}^{-1}\Delta\mathbf{F}\mathbf{F}^{-1})))\nabla_{\mathbf{x}}\delta\vartheta - J(\mathbf{k}\nabla_{\mathbf{x}}\vartheta)(\nabla_{\mathbf{x}}\delta\vartheta(-\mathbf{F}^{-1}\Delta\mathbf{F}\mathbf{F}^{-1})) \\ &= J(\mathbf{k}(\nabla_{\mathbf{x}}\vartheta(\Delta\mathbf{F}\mathbf{F}^{-1})))\nabla_{\mathbf{x}}\delta\vartheta + J(\mathbf{k}\nabla_{\mathbf{x}}\vartheta)(\nabla_{\mathbf{x}}\delta\vartheta(\Delta\mathbf{F}\mathbf{F}^{-1})). \end{aligned} \quad (\text{B.12})$$

Operating in Eq.(B.11), one can express

$$\begin{aligned} \mathcal{I}_{\mathbf{F}} &= J\left(\mathbf{K}_{e,ij}\left((\nabla_{\mathbf{x}}\vartheta)_k\left(\Delta\mathbf{F}_{kl}\mathbf{F}_{lj}^{-1}\right)\right)(\nabla_{\mathbf{x}}\delta\vartheta)_i + J(\mathbf{K}_{e,jm}(\nabla_{\mathbf{x}}\vartheta)_m)\left((\nabla_{\mathbf{x}}\delta\vartheta)_k\left(\Delta\mathbf{F}_{kl}\mathbf{F}_{lj}^{-1}\right)\right)\right. \\ &= \left. J\left(\mathbf{K}_{e,ij}(\nabla_{\mathbf{x}}\vartheta)_k\mathbf{F}_{lj}^{-1}(\nabla_{\mathbf{x}}\delta\vartheta)_i + \mathbf{K}_{e,jm}(\nabla_{\mathbf{x}}\vartheta)_m(\nabla_{\mathbf{x}}\delta\vartheta)_k\mathbf{F}_{lj}^{-1}\right)\Delta\mathbf{F}_{kl}\right) \\ &\quad \underbrace{\mathcal{I}_{\mathbf{F},kl}^*}_{\mathcal{I}_{\mathbf{F},kl}^*}. \end{aligned} \quad (\text{B.13})$$

Based on the previous derivation, the linearization of  $\Delta\mathcal{I}$  yields

$$\Delta\mathcal{I} - ((\mathbf{k}\nabla_{\mathbf{x}}\vartheta)\nabla_{\mathbf{x}}\delta\vartheta)J\mathbf{F}^{-T} : \Delta\mathbf{F} - J\nabla_{\mathbf{x}}\delta\vartheta(\mathbf{k}\nabla_{\mathbf{x}}\Delta\vartheta) + \mathcal{I}_{\mathbf{F}}^* : \Delta\mathbf{F}. \quad (\text{B.14})$$

## References

- [1] Advani S.G., Tucker C.L. (1987) The use of tensors to describe and predict fiber orientation in short fiber composites. *J.Rheol.*, 31:751–784
- [2] Advani S.G., Talreja R. (1993) A continuum approach to determination of elastic properties of short fibre composites. *Mech. Of Compos. Mater.* 29(2):171–183.
- [3] Arif M.F., Meraghni F., Chemisky Y., Despringre N., Robert G. (2014) In situ damage mechanisms investigation of PA66 GF30 composite Effect of relative humidity. *Comp. Part B* 58:487–495.
- [4] Arif M.F., Saintier N., Meraghni F., Fitoussi J., Chemisky Y., Robert G. (2014) Multiscale fatigue damage characterization in short glass fiber reinforced polyamide-66. *Comp. Part B* 61:55–65.
- [5] Bellenger, V., Tcharkhtchi, A., Castaing, P. (2006) Thermal and mechanical fatigue of a PA66/glass fibers composite material. *Int. J. of Fatigue* 28(10):1348–1352.
- [6] A. Bernasconi, F. Cosmi, P.J. Hine (2012) Analysis of fibre orientation distribution in short fibre reinforced polymers: A comparison between optical and tomographic methods. *Composites Science and Technology*, 72(16):2002–2008.
- [7] Boehler, J.P. (1987) Applications of Tensor Functions in Solid Mechanics. CISM Courses and Lectures, vol. 292, Springer.
- [8] Botelho E.C., Figiel L., Rezende M.C., Lauke B. (2003) Mechanical behavior of carbon fiber reinforced polyamide composites. *Comp. Sci. Tech.* 63:18431855.
- [9] B.D. Coleman, W. Noll (1963) The thermodynamics of elastic materials with heat conduction and viscosity. *Archive for Rational Mechanics and Analysis*, 13:167–178.
- [10] Dean A., Reinoso J., Sahraee S., Rolfs R. (2016) An invariant-based anisotropic material model for short fiber-reinforced thermoplastics: coupled thermo-plastic formulation. *Composites Part A: Applied Science and Manufacturing* 90:186–199.

- [11] Dean A., Sahraee S., Reinoso J., Rolfes R. (2016) Finite deformation model for short fiber reinforced composites: Application to hybrid metal-composite clinching joints. *Composite Structures* 151:162-171.
- [12] De Monte, M., Moosbugger, E, Quaresimin, M. (2010) Inuence of temperature and thickness on the off-axis behaviour of short glass bre reinforced polyamide 6.6Quasi-static loading. *Compos: Part A* 41:859-871.
- [13] De Monte, M., Moosbugger, E, Quaresimin, M. (2010) Inuence of temperature and thickness on the off-axis behaviour of short glass bre reinforced polyamide 6.6Cyclic loading. *Compos: Part A* 41:1368-79.
- [14] Eftekhari M., Fatemi A. (2015) Tensile, creep and fatigue behaviors of short fiber reinforced polymer composites at elevated temperatures: a literature survey. *Fatigue Fract. Eng. Mater. Struct.* 38,1395.
- [15] Eftekhari M., Fatemi A. (2016) Tensile behavior of thermoplastic composites including temperature, moisture, and hygrothermal effects. *Polym Test*, 51: 151e64
- [16] Eidel, B., Gruttmann, F. (2003) Elastoplastic orthotropy at finite strains: multiplicative formulation and numerical implementation. *Comput. Mater. Sci.* 28:732-742.
- [17] Eidel, B. (2004) Anisotropic Inelasticity: Modelling, Simulation, Validation. PhD Dissertation, Technischen Universität Darmstadt, Darmstadt, Germany.
- [18] Gasser T.C., Ogden R.W., Holzapfel G.A. (2006) Hyperelastic modelling of arterial layers with distributed collagen fibre orientations. *J R Soc Interface* 3, 1535.
- [19] Feyel F., ChabocheJ.-L. (2000) FE2 multiscale approach for modelling the elastoviscoplastic behaviour of long fibre SiC/Ti composite materials, *Computer Meth. in Appl. Mech. and Eng.*,183:309–330.
- [20] Fu S.Y., Lauke B. (1998) The elastic modulus of misaligned short-fiber-reinforced polymers. *Compos. Sci. Tech.* 58(3):389–400.
- [21] Fu S.Y.,Lauke B., Mai Y.W. (2009) Science and Engineering of Short Fibre Reinforced Polymer Composites. Woodhead Publishing Series in Composites Science and Engineering, ISBN: 978-1-84569-269-8.
- [22] Hine, P.J., Lusti, H.R., Gusev, A.A. (2002) Numerical simulation of the effects of volume fraction, aspect ratio and fibre length distribution on the elastic and thermoelastic properties of short fibre composites. *Comp. Sc. Tech.* 62(10-11):1445-1453.
- [23] Holzapfel G.A., Eberlein R., Wriggers P., Weizsäcker H.W. (1996). A new axisymmetrical membrane element for anisotropic, finite strain analysis of arteries. *Comm. Numer. Met. Eng.* 12:507517.
- [24] Holzapfel G.A, Simo J.C. (1996) A new viscoelastic constitutive model for continuous media at finite thermomechanical changes. *Int J Solids Struct* 33(20):3019–3034.
- [25] Holzapfel G.A., Simo J.C. (1996) Entropy elasticity of isotropic rubber-like solids at finite strains. *Comput. Methods Appl. Mech. Engrg.*, 132:17-44.
- [26] Holzapfel G. A. (2000) Nonlinear solid mechanics. John Wiley & Sons Ltd. ISBN: 978-0-471-82319-3.
- [27] Holzapfel G.A., Gasser T.C. (2001). A viscoelastic model for fiberreinforced composites at finite strains: continuum basis, computational aspects and applications. *Comput. Methods Appl. Mech. Eng.* 190, 43794403.
- [28] Imbrahimbegovic, A., Chorfi, L., Gharzeddine, F. (2001) Thermomechanical coupling at finite elastic strain: Covariant formulation and numerical implementation. *Commun. Numer. Meth. Engng.* 17:275-289.
- [29] Imbrahimbegovic, A., Chorfi, I. (2002) Covariant principal axis formulation of associated coupled thermoplasticity at finite strains and its numerical implementation. *Int J. Solids Struct.* 39:499–528.
- [30] Launay, A., Maitournam, M. H., Marmo, Y., Raoult, I., Szmytka, F. (2011) Cyclic behaviour of short glass bre reinforced polyamide: Experimental study and constitutive equations. *Int. J. Plast.* 27:1267–1293.
- [31] Lion A. (2000) Constitutive modelling in finite thermoviscoplasticity: a physical approach based on nonlinear rheological models. *International Journal of Plasticity* 16, 469–494.
- [32] Lu S.C.H., Pister K.D. (1975) Decomposition of deformation and representation of the free energy function for isotropic thermoelastic solids. *International Journal of Solids and Structures* 11, 927–934.
- [33] Marco Y., Le Saux V., Jégou L., Launay A., Serrano L., Raoult I., Callot S. (2014) Dissipation analysis in SFRP structural samples: Thermomechanical analysis and comparison to numerical simulations. *Int J Fatigue*, 67:142–150.
- [34] Menzel, A., Steinmann, P. (2003) On the spatial formulation of anisotropic multiplicative elasto-plasticity. *Comput. Methods Appl. Mech. Engrg.* 192:3431-3470.
- [35] Miehe, C., Apel, N., Lambrecht, M. (2002) Anisotropic additive plasticity in the logarithmic strain space: modular kinematic formulation and implementation based on incremental minimization principles for standard materials. *Comput. Methods Appl. Mech. Engrg.* 191:5383-5425.
- [36] Mlekusch B. (1999) Thermoelastic properties of short-fibre-reinforced thermoplastics. *Compos Sci Technol*, 59:911–923.
- [37] Mouhmid B., Imad A., Benseddiq N. , Benmedakhene S., Maazouz A. (2006) A study of the mechanical behaviour of a glass fibre reinforced polyamide 6,6: experimental investigation. *Polym. Test.* 25(4):544–552.
- [38] Reese S., Raible T., Wriggers P. (2001) Finite element modelling of orthotropic material behaviour in pneumatic membranes. *Int. J. Solids and Struct.* 38:9525–9544.
- [39] Reese, S. (2003) Meso-macro modelling of fibre-reinforced rubber-like composites exhibiting large elastoplastic deformation. *Int. J. Solids and Struct.* 40(4):951–980.
- [40] Reinoso, J., Blázquez, A. (2016) Application and finite element implementation of 7-parameter shell element for geometrically nonlinear analysis of layered CFRP composites. *Composite Structures*, 139:263–276.
- [41] Sansour C., Kollmann F.G. (2001) Anisotropic formulations for finite strain viscoplasticity, Applications to shells. In: Wall, W.A., Bletzinger, K.-U., Schweizerhof, K. (Eds.), *Proceedings of Trends in Computational Structural Mechanics*. CIMNE, Barcelona, Spain.
- [42] Sansour C., Karsaj I., Soric J. (2007) On a formulation for anisotropic elastoplasticity at finite strains invariant with respect to the intermediate configuration. *J. Mech. Phys. of Sol.* 55:2406-2426.

- [43] Schröder J., Gruttmann F., Löblein J. (2002) A simple orthotropic finite elastoplasticity model based on generalized stressstrain measures. *Comput. Mech.* 30:48–64.
- [44] Schröpfer J. (2011) Spritzgussbauteile aus kurzfaserverstärkten Kunststoffen: Methoden der Charakterisierung und Modellierung zur nichtlinearen Simulation von statischen und crashrelevanten Lastfällen. Dissertation Technischen Universität Kaiserslautern.
- [45] Simo J.C., Miehe C. (1992) Associative coupled thermoplasticity at finite strains: Formulation numerical analysis and implementation. *Comput. Methods Appl. Mech. Engrg.* 98:41-104.
- [46] Spahn, J., Andrä, H., Kabel, M., Muller, R. (2014) A multiscale approach for modeling progressive damage of composite materials using fast Fourier transforms *Comput Method Appl Mech Eng*, 268:871–883.
- [47] Spencer A.J.M. (1971) Theory of invariants, in: A.C. Eringen (Ed.), *Continuum Physics*, vol. 1, Academic Press, New York, 239-353.
- [48] Spencer A.J.M. (2001). A theory of viscoplasticity for fabric-reinforced composites. *Journal of the Mechanics and Physics of Solids* 49, 26672687.
- [49] Thi T.B.N., Morioka M., Yokoyama A., Hamanaka S., Yamashita K., Nonomura C. (2015) Measurement of fiber orientation distribution in injection-molded short-glass- fiber composites using X-ray computed tomography. *J Mater Process Technol*, 219:1–9.
- [50] Truesdell, C., Noll, W. (1965) The nonlinear field theories of mechanics, in: S. Flügge (Ed.), *Encyclopedia of Physics*, vol. III/3, Springer, Berlin.
- [51] Vladimirov, I. N., Pietryga, M. P., Reese, S. (2010) Anisotropic finite elastoplasticity with nonlinear kinematic and isotropic hardening and application to sheet metal forming. *International Journal of Plasticity*; 2010; 0749-6419; Vol. 26, 659-687.
- [52] Vogler, M., Rolfs, R. and Camanho, P.P. (2013) Modeling the inelastic deformation and fracture of polymer composites part I: plasticity model. *Mech.of Mater.* 59:50–64.
- [53] Vogler, M. (2014) Anisotropic Material Models for Fiber Reinforced Polymers. PhD Thesis, Institute of Structural Analysis, Leiniz Universität Hannover, Hannover, Germany.
- [54] Zohdi, T., Wriggers, P. (2001) Aspects of the computational testing of properties of microheterogeneous material samples, *Inter. J. Meth. Eng.*, 50:2573–2599.
- [55] Belmonte, E., De Monte, M., Hoffmann, C., Quaresimin, M. (2017) Damage initiation and evolution in short fiber reinforced polyamide under fatigue loading: Influence of fiber volume fraction, *Composites Part B: Engineering*, 113:331–341.
- [56] Heim, D., Hartmann, M., Neumayer, J., Klotz, C., Ahmet, Ö., Zaremba, S., Drechsler, K. (2013) Novel method for determination of critical fiber length in short fiber carbon/carbon composites by double lap joint, *Composites Part B: Engineering*, 54:365–370.
- [57] Ibanez, F.T., Cicero, S. (2017) Fracture assessment of notched short glass fibre reinforced polyamide 6: An approach from failure assessment diagrams and the theory of critical distances, *Composites Part B: Engineering*, 111:24–133.
- [58] Mortazavian, S., Fatemi, A. (2015) Effects of fiber orientation and anisotropy on tensile strength and elastic modulus of short fiber reinforced polymer composites, *Composites Part B: Engineering*, 72:116–129.
- [59] Ozkan, C., Karsli, N., Aytac, A., Deniz, V. (2014) Short carbon fiber reinforced polycarbonate composites: Effects of different sizing materials, *Composites Part B: Engineering*, 62:30–235.